https://doi.org/10.5194/egusphere-2024-3438
Preprint. Discussion started: 13 January 2025

Identifying Synoptic Controls on Boundary Layer Thermodynamic and Cloud Properties in a Regional Forecast Model

Jordan Eissner[1], David Mechem[1], Yi Jin[2], Virendra Ghate[3], and James Booth[4]

[1]Department of Geography and Atmospheric Sciences, University of Kansas, Lawrence, KS, 66049, USA
[2]Naval Research Laboratory, Monterey, CA, 93943, USA
[3]Argonne National Laboratory, Lemont, IL, 60439, USA
[4]City University of New York, City College and the Graduate Center, New York, NY, 10031, USA

Correspondence: Jordan Eissner (jeissner@ku.edu)

Abstract. Most of our understanding of boundary-layer cloudiness is based on idealized, subtropical, barotropic marine environments, yet boundary-layer clouds exist across a range of conditions. In this study, we investigate marine boundary-layer clouds associated with a midlatitude synoptic cyclone. We use the Naval Research Laboratory's Coupled Ocean/Atmosphere Mesoscale Prediction System (COAMPS) and an automated cold-front-relative analysis framework to explore low cloud properties across a transect from the warm sector, through the cold front, and northwestward into the cold sector. The model credibly captures boundary-layer structure in line with conceptual models. However, the simulated clouds are too thick, with too much liquid water and too little cloud-base drizzle, compared to observations. The transects reveal a shallow, conditionally unstable boundary layer in the warm sector, accompanied by shallow clouds with low liquid water content. The frontal region exhibits forced convection associated with weak stability and upward vertical motion. Northwest of the cold front, the boundary layer is well-mixed with increasing depth and stability. Further northwest in environments of high stability and subsidence, the model produces clouds and associated upward grid-scale vertical motion. We interpret these features as the model's attempt to represent cumulus or mesoscale organization of closed cellular convection typically observed in the wake of midlatitude cyclones. The deep, well-mixed boundary layers and shallow cumulus are maintained by strong surface fluxes, as in cold air outbreaks. Our analysis framework serves as a unique approach to model verification, and our results offer unique insights into cloud and boundary layer evolution throughout a cyclone.

1 Introduction

Boundary layer clouds are large contributors to the global energy budget due to their extensive areal coverage and high albedo. It has been shown that a large amount of the cloud feedback uncertainty in global climate models is due to the misrepresentation of marine low clouds over maritime oceans (Bony and Dufresne, 2005; Zelinka et al., 2016, 2020). Part of the difficulty in understanding and modeling boundary layer cloudiness lies in the stark differences in thermodynamics and dynamics among the different cloud regimes, as well as challenges in representing the continuum of transitions among these regimes across different environments.

https://doi.org/10.5194/egusphere-2024-3438
Preprint. Discussion started: 13 January 2025

Much of our understanding of low cloud behavior and transitions among different cloud regimes has come through study of these clouds in barotropic subtropical regions. In subtropical ocean basins, two well-known mechanisms are used to explain cloudiness transitions. The first is the deepening-warming hypothesis proposed by Bretherton and Wyant (1997). Stratocumulus form east of the semi-permanent high-pressure systems in areas of subsidence, shallow planetary boundary layers (PBL), and cool sea surface temperatures (SST) (Norris and Klein, 2000). As air moves westward and equatorward from the eastern side of the high, it passes over warmer SST, increasing the surface flux, which increases the entrainment rate and deepens the PBL. This tends to decouple the boundary layer, where mixing between the cloud and surface layers is inhibited (Bretherton and Wyant, 1997; Wood and Bretherton, 2004). As potential instability builds at the surface, shallow cumulus can form underneath the stratocumulus. If the stratocumulus become cut off from the surface moisture and dissipate, a transition to broken shallow cumulus occurs (Nicholls, 1984). The second cloud transition mechanism relies on precipitation. Evaporation of drizzle drops from stratocumulus cools and moistens the sub-cloud layer relative to the cloud layer, resulting in a stabilization of the boundary layer (Savic-Jovcic and Stevens, 2008). Again, the boundary layer becomes decoupled, which can dissipate the stratocumulus and drive a transition to broken cumulus clouds.

Low clouds are also associated with midlatitude synoptic cyclones (Boutle et al., 2010; Field and Wood, 2007). Synoptic variability over the midlatitude oceans is much more transient than over the subtropics, especially in winter (Wood et al., 2015; Mechem et al., 2018). Extratropical cyclones frequently traverse the North Atlantic Ocean, following the polar jet stream and producing cloud variability with much shorter timescales than over subtropical oceans (Wang et al., 1999). The PBL structure in midlatitude cyclones is strongly linked to thermal advection and associated large-scale vertical motion. In an idealized, dry simulation of midlatitude cyclones, Sinclair et al. (2010) found that in the warm sector of cyclones, the PBL is stable with an inversion height of ∼500 m, and warm air advection results in negative sensible heat fluxes. In the cold sector, the PBL is well-mixed and unstable, cold air advection results in positive sensible heat fluxes and a deeper boundary layer (∼2.5 km). When moist physics processes are considered, Boutle et al. (2010) found negative surface sensible and latent heat fluxes in the warm sector. Warm advection and convergence are associated with ascent, high clouds, and precipitation along the warm front, extending north, east, and southeast of the cyclone center in the shape of a comma (Boutle et al., 2010; Field and Wood, 2007; Naud et al., 2018b). In the warm sector, a small area fraction of shallow clouds is present (Field and Wood, 2007; Naud et al., 2015). Behind the cold front, positive surface sensible and latent heat fluxes, combined with subsidence associated with the dry intrusion, lead to the formation of boundary layer clouds (Boutle et al., 2010; Field and Wood, 2007). Naud et al. (2018a) examined seven years of observations, yielding ∼1,800 cold fronts in the Eastern North Atlantic (ENA). They found that the post-cold-frontal period had stronger winds and subsidence compared to periods of north or northwesterly flow and subsidence but not associated with a cold front. The post-cold front region is also drier, more unstable, and more turbulent with larger surface fluxes, resulting in clouds that are thicker, with higher cloud cover compared to similar flow and stability conditions but not associated with a cold front.

Various forms of PBL cloud structures have been found in the cold and warm sectors (Field and Wood, 2007; Mechem et al.,

https://doi.org/10.5194/egusphere-2024-3438
Preprint. Discussion started: 13 January 2025

2010; Rémillard and Tselioudis, 2015), but cloudiness transitions in baroclinic environments have not been studied as extensively as in the subtropics. Kazemirad and Miller (2020) applied the Bretherton and Wyant (1997) deepening-warming hypothesis to the stratocumulus to cumulus cloud transition in the region behind cold fronts over the ENA. Lagrangian transports revealed that as air moved southward, latent heat fluxes increased, resulting in more decoupled boundary layers and broken clouds, giving evidence that some cloudiness transitions in midlatitude cyclones are consistent with the deepening-warming mechanism. Jensen et al. (2021) analyzed differences between open and closed-cellular cumulus over ENA and found that open-cellular clouds are associated with stronger cold air advection, surface fluxes, subsidence, and rain rates and deeper boundary layers than those associated with closed-cellular clouds. At high latitudes, continental polar air moving over a relatively warmer sea surface yields strong surface fluxes and what is termed a cold air outbreak (CAO). The resulting boundary layer cloud development and morphology are strongly linked to this surface forcing (Abel et al., 2017; Geerts et al., 2022). The air-sea temperature difference has been shown to be a good predictor of boundary layer cloud fraction on seasonal timescales (McCoy et al., 2017).

Mesoscale and global models struggle to represent midlatitude cloud properties (Bodas-Salcedo et al., 2012) due in part to partially resolved convection processes. In km-scale models, convection is assumed to be resolved, but important motion at the scale of convection, as well as smaller-scale boundary-layer eddies, are not resolved, resulting in errors (Bryan et al., 2003). These models tend to underestimate the boundary layer cloud liquid water content, cloud fraction, and albedo (Abel et al., 2017; Bodas-Salcedo et al., 2012; Field et al., 2017; Nelson et al., 2016; Wyant et al., 2015), but model resolution is not always the issue. Field et al. (2017) simulated a CAO and showed that as the mesoscale model resolution increased, the clouds became even more broken, and the stratocumulus regime disappeared altogether.

This study has two linked objectives: 1. to apply our understanding of boundary-layer clouds, largely relevant to barotropic atmospheres in the subtropics, and expand it to boundary-layer clouds accompanying midlatitude baroclinic synoptic systems; and 2. to evaluate regional numerical weather predictions of forecasts of boundary-layer cloudiness using the Naval Research Laboratory Coupled Ocean/Atmosphere Mesoscale Prediction System (COAMPS, Hodur, 1997). We discuss the observational datasets used and modeling setup in Sect. 2. Section 3 discusses the synoptic setup of our case study. We present our model evaluation results in Sect. 4. In Sect. 5, we analyze model output and observations of boundary layer and cloud properties throughout the cyclone. Finally, in Sect. 6, we discuss the results and conclusions.

2 Data and Methods

2.1 Observations

We use the wealth of continuous observations taken at the Atmospheric Radiation Measurement (ARM) Eastern North Atlantic (ENA) permanent atmospheric observatory deployed on Graciosa Island, Azores. Two intensive observation periods (IOPs) were part of the Aerosol and Cloud Experiments in the Eastern North Atlantic (ACE-ENA) field campaign, taking

https://doi.org/10.5194/egusphere-2024-3438
Preprint. Discussion started: 13 January 2025

place in summer (June-July) 2017 and winter (January-February) 2018 (Wang et al., 2022). The Azores straddles the transition between subtropics and midlatitudes, with large-scale influences from both the Bermuda High and Icelandic Low. In summer, the Bermuda High dominates and PBL clouds are common (Albrecht et al., 1995; Rémillard et al., 2012). The winter season exhibits much greater synoptic variability than the summer, indicated by larger values of 500 hPa geopotential height standard deviations, and cloud patterns are much more transient (Wood et al., 2015). A study that used self-organizing maps to characterize synoptic states over ENA found that in winter, midlatitude cyclone centers tend to remain north of the island, but the associated cold fronts drape across the Azores (see Fig. 8 in Mechem et al., 2018). This makes the Azores region of the ENA an ideal environment to study transient cloud dynamics associated with midlatitude cyclones. This study will focus on a midlatitude synoptic storm system impacting the Azores during 22-29 January 2018. We note that January 2018 was in a positive phase of the North Atlantic Oscillation, so both the Icelandic Low and Bermuda High were stronger than normal. This may in part explain why the storm tracks over this period (and over most of the winter IOP) were farther north (Hurrell, 1995) and may not be fully representative of typical winter storm systems in the northeast Atlantic.

Included in the measurements are the vertically pointing, 35-GHz Ka-Band ARM Zenith Radar (KAZR), which measures the reflectivity and Doppler velocity of clouds and precipitation passing over the site. The KAZR has a range resolution of 30 m and temporal resolution of 4 s. Cloud boundaries are identified by the Active Remote Sensing of Cloud Layers (ARSCL) product, which combines KAZR, ceilometer, and lidar retrievals (Clothiaux et al., 2000; Johnson et al., 2014). Cloud cover was estimated by the ground-based total sky imager (TSI, Long and DeLuisi, 1998; Flynn and Morris, 2000). The 3-Channel Microwave Radiometer (MWR) observes microwave brightness temperatures at 23.8, 30, and 89 GHz. Retrievals from these MWR observations (specifically the MWR retrieval MWRRETv2 product, Gaustad and Zhang, 2021) provide vertically integrated estimates of liquid water path (LWP) at one-minute intervals (Turner, 2007). We use the Synergistic Passive and Active Retrieval of Cloud Properties (SPARCL, Cadeddu et al., 2017, 2020, 2023) product for retrievals of sub-cloud drizzle rates. These rates are estimated using a combination of KAZR and ceilometer retrievals by the methods in O'Connor et al. (2005). We estimate the sub-cloud evaporation as the difference between the cloud base rain rate from SPARCL and the surface rain rate measured by the laser disdrometer, each averaged over 15 min windows to allow the precipitation time to fall to the surface and to yield a robust statistical sample. We also use the SPARCL cloud LWP retrieval, which distinguishes between cloud and drizzle water paths. Although the drizzle water path is small during the case study and the cloud LWP is nearly equal to the MWR LWP, the observed LWPs used are only of the cloud water path. Uncertainties in the cloud LWP retrievals are on the order of 15 $\mathrm{g\,m^{-2}}$ (Cadeddu et al., 2023). Vertical profiles of liquid water potential temperature and total water mixing ratio were calculated using LWP, cloud base height, and cloud top height to solve for the slope of the liquid water mixing ratio profile (the adiabatic liquid water content lapse rate, Γ_l, see Eq. (4) of Zuidema et al., 2005). The liquid water is assumed to be zero at cloud base and increases linearly by Γ_l to cloud top.

Soundings were launched 4 times per day (every 6 h) during the IOP to quantify the thermodynamic profile of the atmosphere (Keeler et al., 2022). Two methods are used to estimate the depth of the planetary boundary layer (PBL). The first approach

https://doi.org/10.5194/egusphere-2024-3438
Preprint. Discussion started: 13 January 2025

uses a Richardson number threshold of 0.5 (Riihimaki et al., 2013). The second approach constitutes our best estimate of PBL depth and is identified by eye based on the inversion in the liquid water potential temperature and total water mixing ratio profiles. The best estimate approach results in an increased PBL depth compared to the Richardson number approach by about 800 m on average throughout the case period. We calculate decoupling indices using the two methods described in Jones et al. (2011) based on the liquid water potential temperature and total water mixing ratio profiles to determine if the boundary layer is well-mixed or thermodynamically distinct to any degree from the surface. Finally, we calculate the estimated inversion strength (EIS) from Wood and Bretherton (2006) to measure the atmospheric stability. We supplement the soundings with the surface meteorology systems (MET) for higher resolution surface observations (Kyrouac et al., 2021). The surface MET observes the 3 m wind, 1 m pressure, and 1.25 m temperature at 1-min intervals. The 1290 MHz radar wind profiler (RWP) measures backscattered radiation which is used to determine the vertical profile of horizontal winds in 15 min averages (Muradyan and Ermold, 2021).

Satellite images and analysis are from the Meteosat-10 geostationary satellite with 4 km resolution. Cloud property retrievals are from Visible Infrared Solar-Infrared Split Window Technique (VISST) algorithm (Minnis et al., 2011) in which LWP is derived from the effective droplet size and visible cloud optical depth, and cloud top height (CTH) is estimated using the emissivity, cloud effective temperature, and a temperature profile obtained from global model output. The cloud coverage is the percentage of cloudy pixels within a 0.5 × 0.5° box. These retrievals use visible imagery and therefore, the analysis is only performed using daytime data when the solar zenith angle is less than 65°.

The European Center for Medium-Range Weather Forecasts (ECMWF) Reanalysis v5 (ERA5, Hersbach et al., 2020) atmospheric reanalysis dataset is also used to explore the spatial patterns of clouds, horizontal wind, temperature, large-scale vertical motion, and surface fluxes surrounding the cyclone and as a semi-independent check on the model simulation. Because the surface flux measurements at the Azores are taken over the island itself, we use the ERA5 surface fluxes over the ocean (0.5° latitude north of the island) to provide representative values to evaluate against the COAMPS-calculated fluxes.

2.2 Configuration of COAMPS simulations

A series of weeklong simulations of a synoptically active period is performed using NRL COAMPS (Hodur, 1997). COAMPS is a mesoscale model based on non-hydrostatic, compressible dynamics. We use a doubly nested domain with two-way interaction, which allows us to perform moderately high-resolution simulations at a large spatial extent while still being computationally and operationally feasible. The coarse grid has a grid spacing of 9 km, 384 × 384 points, and a timestep of 10 s, and the fine mesh has a grid spacing of 3 km and 397 × 397 points (Fig. 1a). The vertical grid uses 45 levels with varying grid spacing. In the boundary layer, the vertical grid spacing ranges from 20 to 80 m; the inversion layer spacing ranges from 80 to 150 m; and the spacing above the inversion ranges from 150 to 1000 m at 10 km (Fig. 1b).

COAMPS initial and boundary conditions are derived from the 6-hourly Global Forecasting System (GFS) 0-h analysis fields,

https://doi.org/10.5194/egusphere-2024-3438
Preprint. Discussion started: 13 January 2025

which have an effective horizontal grid spacing of 27 km. GFS analysis and buoy observations are assimilated into COAMPS using the 3D-variational data assimilation algorithm NRL Atmospheric Variational Data Assimilation System (NAVDAS). The weeklong simulation begins on 22 January 2018 at 00:00 UTC. The first 24 h of the simulation constitutes model spin-up, where observational data are assimilated every 12 h for the first 24 h (two total data update cycles). The model is then run without data assimilation for the next 6 d (144 h, until 29 January 2018 00:00 UTC), with forcing from the GFS only acting via the lateral boundaries on the COAMPS coarse mesh.

COAMPS uses the Kain and Fritsch (1990) parameterization for deep convective processes on the coarse mesh. The convective parameterization is not active on the fine mesh, because a 3 km grid lies in the realm of convective-permitting grid sizes (Prein et al., 2015; Weisman et al., 1997). The radiation scheme is that of Fu and Liou (1992), and surface fluxes are from Louis et al. (1982). The boundary layer and turbulence processes are based on the level 2.5, 1.5-order Mellor and Yamada (1982) parameterization, and the shallow convection is formulated based on Tiedtke et al. (1988).

The COAMPS operational microphysics parameterization is based on the single-moment Rutledge and Hobbs (1983) formulation, with the warm-rain component based on Kessler (1969). This study is predominantly concerned with warm-rain (liquid only) processes. However, COAMPS produces mixed phase clouds with frozen particles making up about 10-50% of the total in-cloud mass in some of the colder convective clouds. Over and south of the Azores region, COAMPS produces very little ice. In situ observations of ice content in wintertime boundary layer clouds at the Eastern North Atlantic site do not exist, so it is uncertain whether frozen particles are expected in these clouds. Though we do not expect this amount of ice to have a significant impact on the forecasts, it could result in an underestimation of liquid water and less warm rain precipitation conversion.

We supplement the Kessler (1969) operational warm-rain microphysics in COAMPS with elements from the Khairoutdinov and Kogan (2000) (KK2000 hereafter) drizzle parameterization. The Kessler (1969) autoconversion, accretion, fall speed, and evaporation expressions are replaced with those from KK2000 to improve the representation of boundary-layer cloud precipitation processes without adding the complexity of a full double-moment scheme. The KK2000 autoconversion expression follows the functional form:

$$(\partial q_r/\partial t)_{auto} = c q_c^{\alpha} N_c^{\beta} \tag{1}$$

where q_c is the cloud water mixing ratio [$\mathrm{kg\ kg^{-1}}$], N_c is the cloud drop concentration [$\mathrm{cm^{-3}}$], and c, α, and β are constants, yielding an autoconversion rate with units [$\mathrm{kg\ kg^{-1}}$]. KK2000 performed a regression analysis on simulated large eddy simulation stratocumulus drop spectra and found the constants to be: c=1350, α=2.47, and β=-1.79. The KK2000 accretion is:

$$(\partial q_r/\partial t)_{accr} = 67(q_c q_r)^{1.15} \tag{2}$$

where q_r is the rain water mixing ratio [$\mathrm{kg\,kg^{-1}}$]. The fall speed is:

$$V_{q_r} = 0.12 r_{vr} - 0.2 \tag{3}$$

where r_{vr} is the mean volume radius of the drizzle drops [μ m] and is estimated as:

$$r_{vr} = (4\pi\rho_w/(3\rho_a))^{-1/3} q_r^{1/3} N_r^{-1/3} \tag{4}$$

where ρ_w is the density of water and ρ_a is the air density. This yields terminal velocities with units [$\mathrm{m\,s^{-1}}$]. Finally, the evaporation is:

$$(\partial q_r/\partial t)_{evap} = 3C_{evap}G(T,p)((4\pi\rho_w/(3\rho_a))^{2/3} q_r^{1/3} N_r^{2/3} S \tag{5}$$

where C_{evap}=0.55, $G(T,p)$ is from the drop radius growth equation as found in Yau and Rogers (1996) or elsewhere. We refer to our implementation of this microphysics parameterization as “KK Lite” because we do not run a full double moment scheme. Rather, we assume a constant cloud (N_c) and drizzle (N_r) drop concentration for the entire simulation. Our control simulation employs the KK Lite parameterization and assumes an N_c of 100 $\mathrm{cm^{-3}}$. This value is broadly representative of maritime conditions, although measurements of cloud condensation nuclei (CCN) at Graciosa Island over the simulation period range from 40 to over 400 $\mathrm{cm^{-3}}$ (0.2% supersaturation). We assume an N_r of 0.01 $\mathrm{cm^{-3}}$, a value based on bin-microphysics large-eddy simulation (LES) findings in marine low clouds (specifically, the System for Atmospheric Modeling – Explicit Microphysics (SAMEX) contributions to Mechem et al., 2012; Rémillard et al., 2017; vanZanten et al., 2011). Although most single-moment microphysical parameterizations functionally relate N_r to the mass field (q_r), we show in Sect. 4 that KK Lite displays only modest sensitivity to the constant values of N we choose. Equations (3) and (4), along with q_r are used to calculate the instantaneous, grid-scale cloud base and surface rain rates in COAMPS. The sub-cloud evaporation is the difference between the cloud base and surface rain rates.

The internally computed COAMPS PBL height is determined by the Richardson number threshold of 0.5. The Richardson number approach is robust but tends to underestimate the inversion height (Wang et al., 2011; Wyant et al., 2010) in cases of a pronounced inversion. As for the observed soundings, a best estimate of the inversion height is found by eye using vertical profiles of potential temperature and water vapor, only over the ENA site. Similar to the observed soundings, at ENA, the best estimate approach results in COAMPS PBL heights that are, on average, higher than using the Richardson number approach (∼400 m higher). We also calculate parameters using the thermodynamic profile, including stability (EIS) and decoupling indices. The subgrid-scale cloud fraction in COAMPS includes a relative humidity threshold at each model level (Slingo, 1987). At grid spacings of 3 km, this is predominantly an all-or-nothing approach (i.e., grid-point cloud fractions of either 0 or 1) but does allow for non-zero cloud fractions at relative humidity values above 70%. For calculations of cloud cover, we use the maximum cloud fraction between 300 and 2000 m at each grid point (maximum overlap assumption).

https://doi.org/10.5194/egusphere-2024-3438
Preprint. Discussion started: 13 January 2025

2.3 Sensitivity experiments

In addition to the baseline COAMPS simulation described above using the KK Lite parameterization, we perform a series of sensitivity experiments. These serve to compare our baseline to the operational Kessler (1969) warm-rain microphysics and the Thompson et al. (2008) parameterization, which is a currently available option in COAMPS. We also evaluate the sensitivity to results to variations in N_c and N_r, specifically with experiments specifying N_c and N_r values of 40 cm^{-3} and 0.1 cm^{-3}, respectively. We also conduct a simulation of KK Lite with both N_c and N_r changed to evaluate the mutual interactions among the two parameters (Stein and Alpert, 1993). The final sensitivity simulation tests the sensitivity to the vertical grid resolution by using an 87-point grid with higher resolution (25 m) throughout the entire boundary layer (0-2 km), though this has no significant impact on the forecasts and results are not shown. A detailed list of the sensitivity experiments is in Table 1.

In addition to the simulations listed in Table 1, we perform another series of COAMPS simulations using the control KK Lite configuration to quantify statistical forecast error. Those simulations all include a 24-h spin-up period, followed by a run of varying lengths. The subsequent simulations begin 12 h after the previous and all finish 29 January 00:00 UTC. This yields 12 total simulations, with twelve 12-h forecasts, eleven 24-h forecasts, ten 36-h forecasts, and so on.

3 Description of case study

Figure 2 shows ERA5 low cloud cover (between approximately 800–1000 hPa) and sea level pressure (SLP) over the ENA every 24 h at 00:00 UTC throughout the simulation period. During the first 48 h of the study period, a low-pressure center is located about 17° north of Graciosa Island. By 00:00 on the 24th, the low becomes zonally elongated, with the associated cold front extending south and southwest from the eastern part of the low center (Fig. 2b). The fronts in Fig. 2a-c are based on the automated frontal identification algorithm, described in Sec. 5.1 and applied to ERA5 data. The cold front shown in Fig. 2a and c does not originate at the low center but otherwise is consistent with the corresponding near-surface temperature field. The Bermuda High center is situated just west of the Azores (Fig. 2b). Sky conditions are nearly overcast along the cold front and at the center of the high, while broken boundary layer clouds are present behind the cold front (Fig. 2c). By 26 January, the center of the high is located over the Azores (Fig. 2d) and continues to move eastward over the final three days of the case study (Fig. 2e,f).

Observations on Graciosa Island during the first 24 h of the study period are characterized by southwesterly winds, broken clouds and a relative minimum in 500 hPa geopotential height and surface pressure (Fig. 3). A cold front passes over ENA around 00:00 UTC on 24 January, indicated by the ERA5 front identification (Fig. 2b). After the cold front passage, the surface pressure is nearly past its minimum, the temperature continues to decrease from the overnight low, and winds change from southwesterly to northwesterly (Fig. 3b,c,d). The KAZR observed precipitating convection along the cold front, and broken, drizzling cumulus with tops at 1.75 km after the cold front passage (Fig. 3e,f). Around 25 January 18:00 UTC, the surface temperature begins to increase, and the winds change to have a southerly component (Fig. 3c,d). The clouds transition from broken cumulus to an unbroken sheet of periodically drizzling stratocumulus with a cloud-top height of approximately 1.5 km (Fig. 3e). The unbroken stratocumulus persists for nearly 48 h, within which the cloud top gradually decreases to 1.3 km. On 28 January, the stratocumulus begins to transition to broken cumulus (Fig. 3e).

When the winds have a southerly wind component (90°-310°; between the green bounds in Fig. 3d), the ENA thermodynamic, cloud, and precipitation quantities may include influences from the island instead of being representative of pure marine conditions (Ghate et al., 2021). Therefore, our evaluation of COAMPS will emphasize the period with northerly wind conditions (24 January 00:00 UTC–25 January 18:00 UTC).

4 Evaluation of COAMPS simulations

We evaluate COAMPS against observations at ENA in a variety of ways. Comparing simulation output, which varies in time and space, to continuous observations at a single location is difficult. Although we have done our best to acknowledge these issues, discrepancies in cloud structures, and cyclone strength and position between the temporal and spatial windows (phase error) may occur. We have chosen to define the COAMPS analysis region as the 144 km × 144 km (48 × 48 points) box centered on Graciosa Island (small green box in Fig. 1) over which we calculate statistics. The wind speed during the case period is at maximum 10 $\mathrm{m\,s^{-1}}$, which corresponds to 36 km of advection in 1 h. Therefore, our COAMPS analysis box roughly corresponds to a 4-h observational window.

COAMPS forecasts of 500 hPa geopotential height and surface pressure for lead times up to 72 h are evaluated against ERA5 reanalysis to understand how COAMPS represents the spatial structure of the synoptic environment. The forecast error for each simulation described in Sect. 2.3 is the mean absolute error (MAE) between ERA5 all COAMPS coarse mesh points regridded to the ERA5 grid. The MAE of the forecast errors at each forecast time is evaluated. As expected, the forecast errors increase as the forecast time increases (Fig. 4). However, COAMPS appears to be representing the large-scale meteorology well, with SLP errors of less than ∼1 hPa and 500 hPa height errors of less than 25 m throughout the entire domain and out to 72 h (Fig. 4). Errors increase at a small rate (or even decrease for the 72-h simulation) potentially due to the dominance of the slowly evolving high pressure system in the later parts of the simulation period.

We next determine how well COAMPS represents the liquid water potential temperature and water vapor mixing ratio profiles compared to the soundings as well as cloud boundary evolution compared to ARSCL cloud boundary retrievals (Fig. 5). During the northerly wind conditions following the passage of the cold front (24 January 00:00 UTC–25 January 18:00 UTC), COAMPS underestimates the temperature profile throughout the lowest 3 km of the atmosphere. Over the same period, COAMPS slightly overestimates the boundary-layer moisture but underestimates the free-tropospheric moisture. COAMPS also underestimates the inversion height and the temperature gradient across the inversion, potentially due to the coarse vertical resolution of the model at this height. The slightly cooler and moister boundary layer results in a cloud base that is too low and a cloud that is too thick. During the southerly wind conditions (after 25 January 18:00 UTC), the boundary layer temperature and moisture are closer to the observed profiles (with the exception of the moisture at 17:30 UTC). For the last two sounding periods, COAMPS overestimates the base of the inversion and again fails to produce a sharp inversion. This results in higher cloud tops and bases than observed, consistent with an overestimate of entrainment in the model perhaps deriving from the crude vertical resolution at the inversion. The near constant state of decoupling at ENA, shown by Rémillard et al. (2012), is better indicated by the moisture profile during the northerly wind conditions, with the temperature profile remaining nearly constant with height beneath the inversion (and D < 0.5 K), and the moisture profile more stratified (D > 1.0 $\mathrm{g\ kg^{-1}}$). However, COAMPS does not represent this stratification in the moisture profile, and it remains fairly well-mixed (D < 0.5 $\mathrm{g\ kg^{-1}}$).

Low level winds can also play a role in boundary layer evolution, so we compare COAMPS, sounding, and Radar Wind Profiler wind speeds throughout the period (Fig. 6). COAMPS represents the low-level wind speeds well compared to observations, but slightly overestimates the near-surface (<500 m) wind speed and underestimates the upper-level wind speed. Boundary layer winds are relatively constant with height and weaken throughout the period. The gradual decrease in wind speeds and boundary layer turbulence corresponds to a gradual decrease in boundary layer height further away from the cold front, as expected.

Figure 7 compares bulk sounding parameters between COAMPS and seven observed soundings during the northerly wind period. All of the COAMPS microphysics sensitivity experiments overestimate stability (EIS) but predict it within ∼1 K (Fig. 7a). All simulations, on average, underestimate the boundary layer height, but KK Lite has the lowest mean absolute error (MAE) and predicts the PBL depth to within 172 m or about 12% (Fig. 7b). The Thompson parameterization underestimates the PBL depth by 192 m and Kessler underestimates it by 187 m, yielding in MAE values for each simulation within 20 m of each other. The substantial underestimate of boundary-layer depth reflects well-known, long-standing bias in regional (and larger-scale) models underestimating the depth of the marine boundary layer inversion (Wyant et al., 2010, 2015) that is predominantly tied to how poorly the model vertical grid represents the inversion. In our case, this error seems reasonable given the vertical grid spacing of ∼100 m at this height. Although we have tested a higher resolution vertical grid, grid spacings of 25 m across the inversion are still too coarse to result in significant improvement of the boundary layer depth. The Kessler parameterization best represents the degree of decoupling, only overestimating decoupling for one sounding (Fig. 7c). The Thompson parameterization also predicts the decoupling index relatively well. As shown in Fig. 5, KK Lite struggles with representing the level of decoupling in the boundary layer, often coupling the boundary layer when observations show decoupling, especially overmixing the moisture profile. However, Kazemirad and Miller (2020) used a threshold of $D_q < 1.6\ \mathrm{g\ kg^{-1}}$ to indicate not-decoupled profiles, making all COAMPS and observed profiles not decoupled by this metric. We characterize the differences in MAE values across the simulations (0.29 K EIS; 20 m for PBL depth; and 0.09 for the decoupling index) as only modest sensitivity to the microphysical parameterization. More precisely, the simulations exhibit a degree of bias relative to the observations, but that bias is only minimally attributable to differences among the microphysical parameterizations. Below we provide an explanation for the differences among the microphysical sensitivity simulations.

https://doi.org/10.5194/egusphere-2024-3438
Preprint. Discussion started: 13 January 2025

Probability distribution functions (PDFs) from COAMPS and the observations are compared over the case study period in Fig. 8. The ENA observations have high temporal resolution but at a single point, so we attempt to find the temporal window over which the observations correspond to a finite spatial domain size. COAMPS PDFs are created from forecast hour 32-64 and a 144 km × 144 km box centered on Graciosa Island. The observed PDFs are created from a temporally equivalent sampling window, accounting for advection (assuming a 10 $\mathrm{m\,s^{-1}}$ wind speed), between 24 January 2018 00:00 UTC to 25 January 2018 18:00 UTC (COAMPS forecast hour 30-66). All variables are conditioned on nonzero elements. In addition, Table 2 compares averages of the variables over this 144 × 144 $\mathrm{km^{-2}}$ ENA region during the northerly wind period of each microphysics parameterization sensitivity simulation.

Relative to the observations, we find that all three COAMPS simulations produce fewer clouds at small LWP values (50-100 g $\mathrm{m^{-2}}$) and more, large-LWP clouds (>200 $\mathrm{g\,m^{-2}}$) (Fig. 8a). With the exception of the Kessler simulation (55.3 vs 54.2 $\mathrm{g\,m^{-2}}$ in Table 2), all of the others considerably overestimate the mean LWP values at the ENA site. In addition, all simulations overestimate the cloud thickness, producing clouds 50-200 m too thick (Table 2). As discussed previously, all simulations underestimate the Richardson-number PBL depth by 200-300 m compared to observations (Table 2). COAMPS also underestimates clouds at low cloud fractions (<0.25) and overestimates cloud fractions of 0.75-1.0 (Fig. 8e), potentially missing some of the broken shallow convective clouds due to the coarse horizontal resolution and instead producing grid-scale convection. Observations of precipitation rate at cloud base and the surface show that nearly all of the precipitation evaporates before reaching the surface (Fig. 8b,d, and Table 2). The COAMPS simulations, on the other hand, underestimate the cloud base rain rate and largely overestimate the surface rain rate, resulting in a large underestimation of sub-cloud evaporation. The KK Lite control simulation produces the largest cloud base rain rate relative to the Kessler and Thompson parameterizations, owing to the suitability of its autoconversion, accretion, and fall speed relations for marine low clouds.

Means over the entire fine mesh domain are compared in the italicized numbers in Table 2 to describe the sensitivity between the different simulations. Many but not all of the differences can be explained by the differences in microphysical parameterizations and assumed parameters. The fraction of the cloud-base precipitation that evaporates depends on the sub-cloud humidity and the shape of the drop-size distribution, with a larger number of smaller drops having greater total surface area and are therefore easily evaporated. For this reason, the KK Lite simulations with N_r = 0.1 $\mathrm{cm^{-3}}$ exhibit a larger fraction of precipitation that is evaporated relative to the other KK Lite simulations. The smaller magnitudes of cloud-base precipitation for the N_r = 0.1 $\mathrm{cm^{-3}}$ simulations are consistent with the smaller raindrops associated with a larger value of N_r having slower sedimentation velocity. Higher evaporation rates result in increased boundary layer stability (Nicholls, 1984), reduced turbulence and entrainment, and a decreased PBL height (Stevens et al., 1998). Both KK Lite parameterizations with N_r = 0.01 $\mathrm{cm^{-3}}$ have the largest sub-cloud evaporation rates and shallowest PBL heights. The Thompson simulation produces the smallest evaporation rates and subsequently has the highest PBL height. This is consistent qualitatively; however, the Kessler simulation has a similar evaporation rate as Thompson but boundary layer heights that are much shallower than Thompson

https://doi.org/10.5194/egusphere-2024-3438
Preprint. Discussion started: 13 January 2025

and closer to the KK Lite simulations, indicating that other factors besides microphysics, such as surface fluxes or large-scale vertical motion, are influencing boundary layer depth. These results show that although COAMPS does not exactly reproduce the observations, it is largely internally consistent with the relationships found in observations.

5 Boundary-layer cloud properties composited on synoptic features

5.1 Cyclone center and frontal identification

The cyclone center and associated fronts are identified in COAMPS using the Bauer et al. (2016) and Naud et al. (2016) algorithms, respectively. The Bauer et al. (2016) algorithm identifies and tracks cyclones using local minima in SLP, which are then filtered by a threshold based on topography, latitude, and season to ensure that the cyclone identified is meaningful. Once cyclone centers are identified, associated fronts are located based on both the 1 km horizontal potential temperature gradient (Hewson, 1998) and 6 h change of the 850 mb wind direction and magnitude (Simmonds et al., 2012). Naud et al. (2016) applies several filters to the frontal locations found by the Hewson (1998) and Simmonds et al. (2012) methods to find the best estimate of warm and cold front locations. The cyclone centers and associated fronts are then tracked over time at 6-h increments (Bauer et al., 2016). Figure 9 shows the objectively identified cyclone center and cold front from the COAMPS simulation at 06:00 UTC on January 24, just after the time of the cold front passage over the Azores. The identified cold front lies in a reasonable position, judging from the location of the cold front on the 1 km potential temperature field. The frontal location is also very similar to the location identified using ERA5 data (similar to Fig. 2b).

A cold-front-centered compositing approach (e.g., Field and Wood, 2007) is used to transform the model output into a cold-front-centered coordinate system. This technique highlights the differences between pre-frontal, frontal, and post-cold front environments and allows for straightforward comparisons among the three regions. This system-relative analysis framework also serves to minimize any phase error the model may have associated with a too slow or too rapid movement of the system. We analyze transects across the cold front to explore the joint variability of cloud and boundary-layer properties (LWP, PBL depth) and meteorological conditions (stability, vertical motion, surface fluxes). The transect passes through Graciosa Island and is perpendicular to the cold front (Fig. 9). A transect width of 111 km is created, and variables parallel to the cold front are averaged along the transect. This approach incorporates more data such that the transect captures more cloudy and precipitating grid points compared to a single line.

We separate grid points in the fine mesh and along the transect between the cold, frontal, and warm sectors. The frontal sector is distinguished as the 150 km ahead of (to the southeast) and behind (to the northwest) the cold front, identified to include the upward vertical motion associated with the front. This also corresponds to the distance of influence that the cold front has on the boundary layer, assuming a boundary layer depth of 3 km (a generous value for the boundary layer depths in this study) and a frontal slope of 1:50. The cold sector is defined by all points to the northwest of the frontal region, and the warm sector includes all points ahead (to the southeast) of the frontal region. The synoptic and thermodynamic variables are composited onto a cold-front-centered framework for eight model forecast times 6 h apart, starting with forecast hour 12 and ending with 54. At hour 12 of the simulation, most of the transect is ahead of the cold front and, therefore, mainly samples the properties of the warm sector. As the cyclone moves over time, the transect captures more of the area further behind the cold front.

5.2 Frontal cross sections

Figure 10 shows a map of COAMPS grid-scale cloud-base vertical velocities and LWP in the fine mesh. Clouds along and ahead of the cold front are organized into a banded structure associated with weak upward motion (Fig. 10d,g). Satellite-derived LWP also shows the banded structure of the clouds along and ahead of the cold front (Fig. 10a). Cellular clouds behind the cold front have high LWP and are associated with strong updrafts in the center with downdrafts on the cell edges, reminiscent of closed-cellular stratocumulus clouds. However, the satellite image suggests that the cold sector clouds are more reminiscent of open cellular convection, with clear centers and cloudy cell walls. We interpret the COAMPS cloud features as the model's attempt at mesoscale cellular organization despite the somewhat coarse grid spacing, as in Mechem and Kogan (2003). In the northwest corner of the domain, the cellular structure transitions to complete overcast conditions, with clouds reminiscent of stratus or stratocumulus (Fig. 10e). These more horizontally homogeneous clouds are associated with near-zero or weak downward motion (Fig. 10h). Toward the end of the analysis period, the cells increase in horizontal size (Fig. 10f). At this time, the satellite shows a transition to a more closed cellular structure (Fig. 10c). Though COAMPS does not show total cloud cover, it still produces clouds reminiscent of closed cellular organization.

Figure 11 shows the median vertical cross sections, composited in 100 km wide bins. The boundary layer in the warm sector is moist and conditionally unstable (i.e., not well-mixed) reminiscent of the trade wind cumulus environment and is characterized by periods of weak ascent and descent. The frontal region has sloped potential temperature and vapor mixing ratio profiles and a narrow band of weak ascent in the lowest 1 km. Behind the cold front, the boundary layer is 10 K cooler, 5 $\mathrm{g\ kg^{-1}}$ drier, and well-mixed with inversion heights of 1.5 km just behind the front and 1.2 km 1500 km behind the front. Subsidence dominates the boundary, inversion, and free tropospheric layers throughout the entire cold sector region.

COAMPS LWP values ahead of the cold front in the warm sector are near zero with only a few instances of broken clouds (Fig. 12a). The cloud cover over the warm sector can be as large as 40%, but this largely represents the subgrid-scale contribution and the resolved cloud cover is only 0-10%. In the frontal region, clouds associated with the frontal convective band have LWPs that range from 50-150 $\mathrm{g\ m^{-2}}$. The 750 km immediately behind the cold front have the largest LWPs with about 50% resolved cloud cover and 80% subgrid scale cloud cover, on average. Further behind the cold front, the LWP is lower, but cloud cover is nearly 100%. This provides evidence that COAMPS is trying to represent the observed cloudiness transition between broken, stronger convective clouds close to the front and closed-cellular stratocumulus clouds further behind and closer to the high (Fig. 3).

SSTs are 288 K in the northern part of the fine mesh and increase southward to 293 K in the southern portion of the fine mesh (not shown). This leads to sensible heat fluxes of <5 W m^{-2} in the warm sector where warm air flows over relatively warm water, increasing into the cold sector to 50-150 W m^{-2}, where cold air flows over relatively warm water (Fig. 12b). The latent heat fluxes are over double the magnitude of the sensible heat fluxes and follow the same pattern, ranging from 10-90 W m^{-2} in the warm sector and increasing to as much as 300 W m^{-2} 750 km behind the cold front. Both the sensible and latent heat fluxes in this case are much stronger than in other studies of boundary-layer clouds over the subtropics and midlatitudes. LES intercomparisons for two DYCOMS-II cases yielded sensible and latent heat fluxes of 15 and 115 W m^{-2} (RF01, Stevens et al., 2005), and 16 and 93 W m^{-2} (RF02, Ackerman et al., 2009), respectively. An LES study of stratocumulus over the southeast Pacific during the VOCALS-Rex field campaign calculated sensible and latent heat fluxes of 4-8 and 55-70 W m^{-2} (Mechem et al., 2012). Over the North Atlantic, sensible and latent heat fluxes during the ASTEX campaign ranged from -15 to +15 and 100-150 W m^{-2} (Bretherton et al., 1995) in largely quiescent conditions dominated by the Bermuda High and trade winds (Albrecht et al., 1995). The larger surface fluxes in our study, particularly associated with the cooler air in the post-cold-frontal regions, suggests that cyclones substantially influence the surface fluxes, and the cold sector is much more closely related to the environments of cold air outbreaks (CAO) than the environments in which trade wind cumulus form. The peak in surface fluxes about 750 km behind the cold front is also associated with a peak in LWP, in agreement with CAO studies which also find a transition from closed cell to open cellular clouds as the environment becomes more dynamic and the air-sea temperature difference increases (McCoy et al., 2017; Naud et al., 2018a).

The inversion strength and boundary layer height generally follow the pattern of surface fluxes, with shallow PBL depth and weak stability ahead of the cold front and increasing PBL depth and stability behind the cold front (Fig. 12c). Despite strong subsidence in the cold sector, the boundary layer remains deep, suggesting that the PBL depth is maintained by the strong surface fluxes (Sinclair et al., 2010) and associated shallow convection. Precipitation is sporadic and most likely to occur within 750 km behind the front (Fig. 12d). The boundary layer is also most likely to be decoupled within 500 km of the front, downwind from or where the majority of the precipitation occurs, as expected.

To further generalize the findings from the transects, we create box and whisker plots of the properties in each sector along the transects (Fig. 13). This figure highlights the drastic differences between the quiescent environmental conditions in the warm sector and the much more turbulent and stable conditions of the post-cold frontal environment. Compared to the COAMPS warm sector, the cold sector has much deeper PBLs, higher stability, and stronger surface sensible and latent heat fluxes. The frontal sector is associated with the values of PBL depth, stability and surface fluxes in between those of the warm and cold sectors. The distribution of COAMPS properties from each sector are compared to ENA observations. COAMPS represents the properties of each sector relative to the other sectors correctly, with the largest median values of all 4 variables in the cold sector, smallest median values in the warm sector, and the frontal sector distribution somewhere in between. The boundary layer height discrepancies between COAMPS and the observations in each sector are likely due to the Richardson number not being a good measure of the boundary layer depth in the conditionally unstable warm sector or during instances where the cold sector is decoupled.

Box and whisker plots of the cloud properties in each sector are also presented (Fig. 14). COAMPS produces the widest range and highest LWPs in the cold sector, with values sometimes exceeding 500 $\mathrm{g\,m^{-2}}$, and the smallest LWPs in the warm sector. COAMPS clout top heights in the cold and frontal sectors are very similar, ranging from about 1.5-2 km, and are much higher than the warm sector top heights, which are only around 500 m. The cold sector also has the largest cloud coverage, ranging from about 60-100%. The majority of the warm sector only has about 20% or less cloud coverage. ENA observations show that COAMPS overestimates the LWP (Fig. 8), but throughout the entire cold sector (Fig. 14a), satellite LWP retrievals show that COAMPS reproduces the distribution of clouds well, with only slightly too many high-LWP clouds, compared to the observations. Satellite retrievals indicate that the COAMPS cloud cover is too large (Fig. 14c), with the observations suggesting a more broken cloud field. On the other hand, we previously showed that that resolved-scale cloud coverage is underproduced (Fig. 10, 12a), suggesting that the subgrid-scale cloud fraction parameterization is too aggressive when adding cloud cover to subsaturated regions. COAMPS also underestimates the LWP, height, and coverage of warm sector clouds, which probably is largely tied to the struggle with representing broken cloud fields on a 3-km horizontal grid. Overall, these results are encouraging that COAMPS is better able to represent the boundary layer and cloud properties in this system-relative context as compared to what the point-by-point comparisons with the observations would suggest.

To illustrate the relationship between cloud properties and variables representative of large-scale environmental conditions, we average 144 × 144 $\mathrm{km^2}$ boxes throughout the fine mesh at 6-h intervals between forecast hour 12 and 54, ending when the post cold front region begins to include areas of southerly winds. These regions are then separated into cold, frontal, and warm sectors. Figure 15 plots the mean liquid water content for each of these regions in a parameter space of stability (EIS) and 2500 m vertical motion, taken in the free troposphere and which we take to represent the large-scale vertical motion. Warm-sector clouds are characterized by small LWP and are associated with weak stability and vertical motion. We take these to be the model's attempt at representing cumulus cloud fields (While the EIS can be below zero in the warm sector, it doesn't mean that the profile is absolutely unstable. Rather, the negative EIS is likely because many profiles in the warm sector are conditionally unstable with little to no capping inversion and weak lower tropospheric stability (LTS, Klein and Hartmann, 1993), making the method inapplicable in these cases.) Clouds in the frontal sector are associated with weak stability and form in areas of both ascent and descent associated with the frontal circulation. They have much higher liquid water contents than clouds over the warm sector. Cold-sector clouds characterized by large values of LWP tend to be located just behind the frontal zone. Like the frontal clouds, these post-frontal clouds with large LWP can occur in any vertical motion condition and are associated with weak stability, which allows the partially resolved cloudy updrafts to grow to sufficient depth to yield large values of LWP. Further behind the cold front, the EIS is larger, and the clouds are in an environment dominated by large-scale subsidence, reminiscent of a stratocumulus-topped boundary layer. Although the boundary layer clouds do cluster into certain environments (i.e., stronger clouds with larger LWP clustering in areas weak stability and clouds with low LWP forming in high stability and subsidence), there is no meaningful statistical relationship between them. These findings support the conclusions of Myers and

https://doi.org/10.5194/egusphere-2024-3438
Preprint. Discussion started: 13 January 2025

Norris (2013) and De Szoeke et al. (2016) of no instantaneous relationships among boundary-layer cloudiness, stability, and vertical motion.

6 Conclusions

Most of our understanding of boundary-layer clouds comes from observational and idealized studies over the subtropical and trade regions, yet boundary-layer clouds are also prevalent in midlatitude baroclinic synoptic systems. In this study, we use the COAMPS regional forecast model to explore low cloud properties and behavior during a multi-day period in the warm sector, cold-frontal region, and post-frontal cold sectors of a midlatitude synoptic system over the Eastern North Atlantic (ENA). We have composited COAMPS output and observations relative to the surface low and cold front identified by the Naud et al. (2016) automated frontal detection algorithm. We find that although the COAMPS forecast does not exactly match point-to-point with the observations at ENA, COAMPS credibly represents the different cloud regimes found over ENA, including the cloudiness transitions and associated differences in thermodynamic properties across the front.

Our main findings are as follows:

- The thermodynamic and dynamic properties of the cold and warm sectors differ dramatically, with cold sectors exhibiting much stronger subsidence, stability, and surface fluxes, and a deeper boundary layer topped by thicker clouds and greater cloud cover, relative to the warm sector;
- Most of the boundary layer clouds in the COAMPS simulations are associated with grid-scale vertical motions that are larger than individual clouds but reminiscent of the mesoscale cloud structures (cloud ensembles) observed in the case;
- Clouds in the post-cold-frontal regime exhibit similar properties to clouds in cold air outbreaks;
- Model biases in cloud properties relative to observations are not explained by differences in microphysics parameterization.

Warm sector clouds in the model are associated with shallow, unstable boundary layers, weak vertical motion, and weak surface fluxes. These clouds tend to have lower values of liquid water than clouds in the frontal and cold sectors. The frontal sector has weak stability but stronger upward low-level vertical motion than the warm sector, yielding a small cloud fraction but with clouds of substantial LWP. Clouds in the cold sector occasionally precipitate and form mostly within 1000 km behind the cold front in environments of high stability, a mostly well-mixed boundary-layer capped by a strong inversion, and strong sensible and latent heat fluxes. Some of these properties are reminiscent of the subtropical marine environment, including large-scale subsidence, high stability, and a well-mixed boundary layer, characteristic of an environment that supports the formation of stratocumulus clouds (Norris and Klein, 2000). These transitions in thermodynamic properties and vertical motion are reflected in a cloudiness transition from the more broken cloud field near the front to a higher-cloud-fraction regime reminiscent of closed cellular stratocumulus further behind the cold front. These transitions are present both in observations and transects through the COAMPS domain. However, the cold sector differs from the barotropic environment by having strong temperature and moisture surface fluxes that are much stronger than those found over subtropical ocean basins (cf. Ackerman et al., 2009; Stevens et al., 2005) or quiescent midlatitude marine conditions (Bretherton et al., 1995). In COAMPS, the large surface fluxes appear to be responsible for driving resolved vertical motions and associated clouds. Ultimately, the cloud features in the model organize into patterns characteristic of closed cellular mesoscale convection. This is similar to the interpretation of Mechem and Kogan (2003), who argued that the grid-scale cloud and vertical velocity features at mesoscale-model grid spacings represented cloud ensembles and the emergence of mesoscale organization. Specifically, we interpret the cloudy cells that COAMPS produces as mesoscale organization of the broken cumulus that were observed by the KAZR after the cold front passage and are typically found in the wake of midlatitude cyclones (Field and Wood, 2007; Naud et al., 2018a) and in cold air outbreaks (Geerts et al., 2022; McCoy et al., 2017). Despite representing the large-scale meteorology well, the COAMPS thermodynamic profiles during the northerly wind period at ENA are slightly too cool and moist, which results in clouds with a lower cloud base and larger thickness compared to observations. COAMPS also has a systematic bias in underestimating the boundary layer height by around 200 m (Wang et al., 2011; Wyant et al., 2010, 2015), likely a result of both the coarse vertical grid spacing and an underestimation of entrainment.

COAMPS appears to overestimate the strength and coverage of this grid-scale convection but underestimates the amount of stratiform clouds (those occurring with LWPs of $\sim 100\ \mathrm{g\,m^{-2}}$ and thicknesses of 0.5 km) further behind the cold front. Mesoscale modeling studies of cold air outbreak events also struggle to produce stratiform clouds even though cloudiness in the downwind cumulus regime are well represented (Abel et al., 2017; Field et al., 2014). Future analyses will focus on the properties associated with the transition to stratocumulus during southerly flows and why COAMPS struggles to represent this cloud regime. We expect that forecasts may improve with improvements to the boundary layer parameterization (Field et al., 2014) and horizontal resolution, so to not overrepresent grid-scale convection associated with instability driven by large surface fluxes.

All simulations overestimate the LWP and underestimate precipitation and sub-cloud evaporation. This result is opposite to other findings, which report an underestimation of boundary layer cloud LWP and cloud thickness and overestimation of precipitation in subtropical domains (e.g., Nelson et al., 2016; Wang et al., 2011). We speculate the reason for this discrepancy is related to the important difference between these low clouds in the post-cold-frontal region and subtropical stratocumulus whereby the strong surface fluxes associated with substantial grid-point vertical motions are less present in marine subtropical environments where surface fluxes are weaker. In this sense, the post-frontal low clouds have a strong element of similarity with clouds associated with cold-air outbreaks.

We have tested the sensitivity of cloud and boundary layer properties to different microphysics parameterization with varying parameters. The replacement of Kessler (1969) warm rain microphysics with our KK Lite parameterization improves forecasts of precipitation and boundary layer depth without adding any computational costs. Changing the microphysical parameters in KK Lite results in relationships largely internally consistent with those found in observations but does not fix the biases relative to the observations.

In this work, we demonstrate that the analysis method provides a pathway to compare boundary-layer cloudiness forecasts against observations in the context of the different sectors of midlatitude cyclones and in a manner that minimizes errors associated with misplacement of the cyclone center and frontal structures (i.e., phase error). We provide insights into the connections between boundary layer, cloud, and synoptic properties throughout the cyclone, which can be used to inform modelers.

Code and data availability. Analysis codes are available at https://github.com/jeissner/COAMPS-transect-analysis. Questions about the software can be addressed to the corresponding author. All ARM data sets from ENA used in this study are available through the ARM discovery website: https://adc.arm.gov/discovery/#/results/site_code::ena. ERA5 reanalysis can be downloaded from the ECMWF Climate Data Store: https://cds.climate.copernicus.eu/datasets.

Author contributions. JME and DBM jointly conceived the experimental design and writing of the paper. JME conducted the simulations, conducted the analysis of both model output and observations, and made the figures. YJ assisted with the model, providing data for model ingest, contributed to experimental design, and contributed to writing the manuscript. VPG contributed observational retrieval products, scientific interpretation, and contributed with writing the manuscript. JFB provided invaluable contributions to the automated synoptic ID component of the study.

Competing interests. The authors declare that they have no conflict of interest.

Acknowledgements. Authors Eissner and Mechem were supported by ONR grant N00014-20-1-2519. We also acknowledge partial support from U.S. Department of Energy Atmospheric Systems Research Grants DE-SC0016522 and DE–SC0023083. This research is partially supported by the Office of Naval Research program element 0602435N (author Jin). Author Ghate was supported by the U.S. Department of Energy's (DOE) Atmospheric System Research (ASR), an Office of Science, Office of Biological and Environmental Research (BER) program under Contract DE-AC02-06CH11357 awarded to the Argonne National Laboratory. Author Booth was partially funded by NOAA Award NA19OAR4310076. This work was performed at the HPC facilities operated by the Center for Research Computing at the University of Kansas supported in part through the National Science Foundation MRI Award #2117449.

References

Abel, S. J., Boutle, I. A., Waite, K., Fox, S., Brown, P. R. A., Cotton, R., Lloyd, G., Choularton, T. W., and Bower, K. N.: The Role of Precipitation in Controlling the Transition from Stratocumulus to Cumulus Clouds in a Northern Hemisphere Cold-Air Outbreak, Journal of the Atmospheric Sciences, 74, 2293–2314, https://doi.org/10.1175/JAS-D-16-0362.1, 2017.

Ackerman, A. S., vanZanten, M. C., Stevens, B., Savic-Jovcic, V., Bretherton, C. S., Chlond, A., Golaz, J.-C., Jiang, H., Khairoutdinov, M., Krueger, S. K., Lewellen, D. C., Lock, A., Moeng, C.-H., Nakamura, K., Petters, M. D., Snider, J. R., Weinbrecht, S., and Zulauf, M.: Large-Eddy Simulations of a Drizzling, Stratocumulus-Topped Marine Boundary Layer, Monthly Weather Review, 137, 1083–1110, https://doi.org/10.1175/2008MWR2582.1, 2009.

Albrecht, B. A., Bretherton, C. S., Johnson, D., Scubert, W. H., and Frisch, A. S.: The Atlantic Stratocumulus Transition Experiment—ASTEX, Bulletin of the American Meteorological Society, 76, 889–904, https://doi.org/10.1175/1520-0477(1995)076<0889:TASTE>2.0.CO;2, 1995.

Bauer, M., Tselioudis, G., and Rossow, W. B.: A New Climatology for Investigating Storm Influences in and on the Extratropics, Journal of Applied Meteorology and Climatology, 55, 1287–1303, https://doi.org/10.1175/JAMC-D-15-0245.1, 2016.

Bodas-Salcedo, A., Williams, K. D., Field, P. R., and Lock, A. P.: The Surface Downwelling Solar Radiation Surplus over the Southern Ocean in the Met Office Model: The Role of Midlatitude Cyclone Clouds, Journal of Climate, 25, 7467–7486, https://doi.org/10.1175/JCLI-D-11-00702.1, 2012.

Bony, S. and Dufresne, J.: Marine boundary layer clouds at the heart of tropical cloud feedback uncertainties in climate models, Geophysical Research Letters, 32, 2005GL023 851, https://doi.org/10.1029/2005GL023851, 2005.

Boutle, I. A., Beare, R. J., Belcher, S. E., Brown, A. R., and Plant, R. S.: The Moist Boundary Layer under a Mid-latitude Weather System, Boundary-Layer Meteorology, 134, 367–386, https://doi.org/10.1007/s10546-009-9452-9, 2010.

Bretherton, C. S. and Wyant, M. C.: Moisture Transport, Lower-Tropospheric Stability, and Decoupling of Cloud-Topped Boundary Layers, Journal of the Atmospheric Sciences, 54, 148–167, https://doi.org/10.1175/1520-0469(1997)054<0148:MTLTSA>2.0.CO;2, 1997.

Bretherton, C. S., Austin, P., and Siems, S. T.: Cloudiness and Marine Boundary Layer Dynamics in the ASTEX Lagrangian Experiments. Part II: Cloudiness, Drizzle, Surface Fluxes, and Entrainment, Journal of the Atmospheric Sciences, 52, 2724–2735, https://doi.org/10.1175/1520-0469(1995)052<2724:CAMBLD>2.0.CO;2, 1995.

Bryan, G. H., Wyngaard, J. C., and Fritsch, J. M.: Resolution Requirements for the Simulation of Deep Moist Convection, Monthly Weather Review, 131, 2394–2416, https://doi.org/10.1175/1520-0493(2003)131<2394:RRFTSO>2.0.CO;2, 2003.

Cadeddu, M. P., Marchand, R., Orlandi, E., Turner, D. D., and Mech, M.: Microwave Passive Ground-Based Retrievals of Cloud and Rain Liquid Water Path in Drizzling Clouds: Challenges and Possibilities, IEEE Transactions on Geoscience and Remote Sensing, 55, 6468–6481, https://doi.org/10.1109/TGRS.2017.2728699, 2017.

Cadeddu, M. P., Ghate, V. P., and Mech, M.: Ground-based observations of cloud and drizzle liquid water path in stratocumulus clouds, Atmospheric Measurement Techniques, 13, 1485–1499, https://doi.org/10.5194/amt-13-1485-2020, 2020.

Cadeddu, M. P., Ghate, V. P., Turner, D. D., and Surleta, T. E.: Boundary layer moisture variability at the Atmospheric Radiation Measurement (ARM) Eastern North Atlantic observatory during marine conditions, Atmospheric Chemistry and Physics, 23, 3453–3470, https://doi.org/10.5194/acp-23-3453-2023, 2023.

Clothiaux, E. E., Ackerman, T. P., Mace, G. G., Moran, K. P., Marchand, R. T., Miller, M. A., and Martner, B. E.: Objective Determination of Cloud Heights and Radar Reflectivities Using a Combination of Active Remote Sensors at the ARM CART Sites, Journal of Applied Meteorology, 39, 645–665, https://doi.org/10.1175/1520-0450(2000)039<0645:ODOCHA>2.0.CO;2, 2000.

De Szoeke, S. P., Verlinden, K. L., Yuter, S. E., and Mechem, D. B.: The Time Scales of Variability of Marine Low Clouds, Journal of Climate, 29, 6463–6481, https://doi.org/10.1175/JCLI-D-15-0460.1, 2016.

Field, P. R. and Wood, R.: Precipitation and Cloud Structure in Midlatitude Cyclones, Journal of Climate, 20, 233–254, https://doi.org/10.1175/JCLI3998.1, 2007.

Field, P. R., Cotton, R. J., McBeath, K., Lock, A. P., Webster, S., and Allan, R. P.: Improving a convection-permitting model simulation of a cold air outbreak, Quarterly Journal of the Royal Meteorological Society, 140, 124–138, https://doi.org/10.1002/qj.2116, 2014.

Field, P. R., Brozˇková, R., Chen, M., Dudhia, J., Lac, C., Hara, T., Honnert, R., Olson, J., Siebesma, P., De Roode, S., Tomassini, L., Hill, A., and McTaggart-Cowan, R.: Exploring the convective grey zone with regional simulations of a cold air outbreak, Quarterly Journal of the Royal Meteorological Society, 143, 2537–2555, https://doi.org/10.1002/qj.3105, 2017.

Flynn, D. and Morris, V.: tsiskycover (b1), https://doi.org/10.5439/1992207, artwork Size: 1992207 Pages: 1992207, 2000.

Fu, Q. and Liou, K. N.: On the Correlated k -Distribution Method for Radiative Transfer in Nonhomogeneous Atmospheres, Journal of the Atmospheric Sciences, 49, 2139–2156, https://doi.org/10.1175/1520-0469(1992)049<2139:OTCDMF>2.0.CO;2, 1992.

Gaustad, K. and Zhang, D.: mwrret2turn.c1, https://doi.org/10.5439/1566156, 2021.

Geerts, B., Giangrande, S. E., McFarquhar, G. M., Xue, L., Abel, S. J., Comstock, J. M., Crewell, S., DeMott, P. J., Ebell, K., Field, P., Hill, T. C. J., Hunzinger, A., Jensen, M. P., Johnson, K. L., Juliano, T. W., Kollias, P., Kosovic, B., Lackner, C., Luke, E., Lüpkes, C., Matthews, A. A., Neggers, R., Ovchinnikov, M., Powers, H., Shupe, M. D., Spengler, T., Swanson, B. E., Tjernström, M., Theisen, A. K., Wales, N. A., Wang, Y., Wendisch, M., and Wu, P.: The COMBLE Campaign: A Study of Marine Boundary Layer Clouds in Arctic Cold-Air Outbreaks, Bulletin of the American Meteorological Society, 103, E1371–E1389, https://doi.org/10.1175/BAMS-D-21-0044.1, 2022.

Ghate, V. P., Cadeddu, M. P., Zheng, X., and O'Connor, E.: Turbulence in The Marine Boundary Layer and Air Motions Below Stratocumulus Clouds at the ARM Eastern North Atlantic Site, Journal of Applied Meteorology and Climatology, https://doi.org/10.1175/JAMC-D-21-0087.1, 2021.

Hersbach, H., Bell, B., Berrisford, P., Hirahara, S., Horányi, A., Muñoz-Sabater, J., Nicolas, J., Peubey, C., Radu, R., Schepers, D., Simmons, A., Soci, C., Abdalla, S., Abellan, X., Balsamo, G., Bechtold, P., Biavati, G., Bidlot, J., Bonavita, M., De Chiara, G., Dahlgren, P., Dee, D., Diamantakis, M., Dragani, R., Flemming, J., Forbes, R., Fuentes, M., Geer, A., Haimberger, L., Healy, S., Hogan, R. J., Hólm, E., Janisková, M., Keeley, S., Laloyaux, P., Lopez, P., Lupu, C., Radnoti, G., De Rosnay, P., Rozum, I., Vamborg, F., Villaume, S., and Thépaut, J.: The ERA5 global reanalysis, Quarterly Journal of the Royal Meteorological Society, 146, 1999–2049, https://doi.org/10.1002/qj.3803, 2020.

Hewson, T. D.: Objective fronts, Meteorological Applications, 5, 37–65, https://doi.org/10.1017/S1350482798000553, 1998.

Hodur, R. M.: The Naval Research Laboratory's Coupled Ocean/Atmosphere Mesoscale Prediction System (COAMPS), Monthly Weather Review, 125, 1414–1430, https://doi.org/10.1175/1520-0493(1997)125<1414:TNRLSC>2.0.CO;2, 1997.

Hurrell, J. W.: Decadal Trends in the North Atlantic Oscillation: Regional Temperatures and Precipitation, Science, 269, 676–679, https://doi.org/10.1126/science.269.5224.676, 1995.

Jensen, M. P., Ghate, V. P., Wang, D., Apoznanski, D. K., Bartholomew, M. J., Giangrande, S. E., Johnson, K. L., and Thieman, M. M.: Contrasting characteristics of open- and closed-cellular stratocumulus cloud in the eastern North Atlantic, Atmospheric Chemistry and Physics, 21, 14 557–14 571, https://doi.org/10.5194/acp-21-14557-2021, 2021.

Johnson, K., Giangrande, S., and Toto, T.: KAZRARSCL-c0-All-inclusive data stream, https://doi.org/10.5439/1393437, 2014.

Jones, C. R., Bretherton, C. S., and Leon, D.: Coupled vs. decoupled boundary layers in VOCALS-REx, Atmospheric Chemistry and Physics, 11, 7143–7153, https://doi.org/10.5194/acp-11-7143-2011, 2011.

Kain, J. S. and Fritsch, J. M.: A One-Dimensional Entraining/Detraining Plume Model and Its Application in Convective Parameterization, Journal of the Atmospheric Sciences, 47, 2784–2802, https://doi.org/10.1175/1520-0469(1990)047<2784:AODEPM>2.0.CO;2, 1990.

Kazemirad, M. and Miller, M. A.: Summertime Post-Cold-Frontal Marine Stratocumulus Transition Processes over the Eastern North Atlantic, Journal of the Atmospheric Sciences, 77, 2011–2037, https://doi.org/10.1175/JAS-D-19-0167.1, 2020.

Keeler, E., Burk, K., and Kyrouac, J.: Balloon-borne sounding system (BBSS), WNPN output data, https://doi.org/10.5439/1595321, 2022.

Kessler, E.: On the Distribution and Continuity of Water Substance in Atmospheric Circulations, in: On the Distribution and Continuity of Water Substance in Atmospheric Circulations, pp. 1–84, American Meteorological Society, Boston, MA, ISBN 978-1-935704-36-2, https://doi.org/10.1007/978-1-935704-36-2_1, 1969.

Khairoutdinov, M. and Kogan, Y.: A New Cloud Physics Parameterization in a Large-Eddy Simulation Model of Marine Stratocumulus, Monthly Weather Review, 128, 229–243, https://doi.org/10.1175/1520-0493(2000)128<0229:ANCPPI>2.0.CO;2, 2000.

Klein, S. A. and Hartmann, D. L.: The Seasonal Cycle of Low Stratiform Clouds, Journal of Climate, 6, 1587–1606, https://doi.org/10.1175/1520-0442(1993)006<1587:TSCOLS>2.0.CO;2, 1993.

Kyrouac, J., Shi, Y., and Tuftedal, M.: met.b1, https://doi.org/10.5439/1786358, 2021.

Long, C. and DeLuisi, J.: Development of an Automated Hemispheric Sky Imager for Cloud Fraction Retrievals, in: Proceedings 10th Symposium on Meteorological Observations and Instrumentation,, Phoenix, AZ, 1998.

Louis, J.-F., Tiedtke, M., and Geleyn, J.-F.: A short history of the PBL parameterization at ECMWF, in: Workshop on Planetary Boundary Layer parameterization, 25-27 November 1981, pp. 59–79, ECMWF, Shinfield Park, Reading, 1982.

McCoy, I. L., Wood, R., and Fletcher, J. K.: Identifying Meteorological Controls on Open and Closed Mesoscale Cellular Convection Associated with Marine Cold Air Outbreaks, Journal of Geophysical Research: Atmospheres, 122, https://doi.org/10.1002/2017JD027031, 2017.

Mechem, D. B. and Kogan, Y. L.: Simulating the Transition from Drizzling Marine Stratocumulus to Boundary Layer Cumulus with a Mesoscale Model, Monthly Weather Review, 131, 2342–2360, https://doi.org/10.1175/1520-0493(2003)131<2342:STTFDM>2.0.CO;2, 2003.

Mechem, D. B., Kogan, Y. L., and Schultz, D. M.: Large-Eddy Observation of Post-Cold-Frontal Continental Stratocumulus, Journal of the Atmospheric Sciences, 67, 3368–3383, https://doi.org/10.1175/2010JAS3389.1, 2010.

Mechem, D. B., Yuter, S. E., and De Szoeke, S. P.: Thermodynamic and Aerosol Controls in Southeast Pacific Stratocumulus, Journal of the Atmospheric Sciences, 69, 1250–1266, https://doi.org/10.1175/JAS-D-11-0165.1, 2012.

Mechem, D. B., Wittman, C. S., Miller, M. A., Yuter, S. E., and De Szoeke, S. P.: Joint Synoptic and Cloud Variability over the Northeast Atlantic near the Azores, Journal of Applied Meteorology and Climatology, 57, 1273–1290, https://doi.org/10.1175/JAMC-D-17-0211.1, 2018.

Mellor, G. L. and Yamada, T.: Development of a turbulence closure model for geophysical fluid problems, Reviews of Geophysics, 20, 851–875, https://doi.org/10.1029/RG020i004p00851, 1982.

Minnis, P., Sun-Mack, S., Young, D. F., Heck, P. W., Garber, D. P., Chen, Y., Spangenberg, D. A., Arduini, R. F., Trepte, Q. Z., Smith, W. L., Ayers, J. K., Gibson, S. C., Miller, W. F., Hong, G., Chakrapani, V., Takano, Y., Liou, K.-N., Xie, Y., and Yang, P.: CERES Edition-2 Cloud Property Retrievals Using TRMM VIRS and Terra and Aqua MODIS Data—Part I: Algorithms, IEEE Transactions on Geoscience and Remote Sensing, 49, 4374–4400, https://doi.org/10.1109/TGRS.2011.2144601, 2011.

Muradyan, P. and Ermold, B.: 1290-MHz Radar Wind Profiler: Low Mode Wind Averages, https://doi.org/10.5439/1663214, 2021.

Myers, T. A. and Norris, J. R.: Observational Evidence That Enhanced Subsidence Reduces Subtropical Marine Boundary Layer Cloudiness, Journal of Climate, 26, 7507–7524, https://doi.org/10.1175/JCLI-D-12-00736.1, 2013.

Naud, C. M., Posselt, D. J., and Van Den Heever, S. C.: A CloudSat–CALIPSO View of Cloud and Precipitation Properties across Cold Fronts over the Global Oceans, Journal of Climate, 28, 6743–6762, https://doi.org/10.1175/JCLI-D-15-0052.1, 2015.

Naud, C. M., Booth, J. F., and Del Genio, A. D.: The Relationship between Boundary Layer Stability and Cloud Cover in the Post-Cold-Frontal Region, Journal of Climate, 29, 8129–8149, https://doi.org/10.1175/JCLI-D-15-0700.1, 2016.

Naud, C. M., Booth, J. F., and Lamraoui, F.: Post Cold Frontal Clouds at the ARM Eastern North Atlantic Site: An Examination of the Relationship Between Large-Scale Environment and Low-Level Cloud Properties, Journal of Geophysical Research: Atmospheres, 123, https://doi.org/10.1029/2018JD029015, 2018a.

Naud, C. M., Booth, J. F., Lebsock, M., and Grecu, M.: Observational Constraint for Precipitation in Extratropical Cyclones: Sensitivity to Data Sources, Journal of Applied Meteorology and Climatology, 57, 991–1009, https://doi.org/10.1175/JAMC-D-17-0289.1, 2018b.

Nelson, K. J., Mechem, D. B., and Kogan, Y. L.: Evaluation of Warm-Rain Microphysical Parameterizations in Mesoscale Simulations of the Cloudy Marine Boundary Layer, Monthly Weather Review, 144, 2137–2154, https://doi.org/10.1175/MWR-D-15-0266.1, 2016.

Nicholls, S.: The dynamics of stratocumulus: Aircraft observations and comparisons with a mixed layer model, Quarterly Journal of the Royal Meteorological Society, 110, 783–820, https://doi.org/10.1002/qj.49711046603, 1984.

Norris, J. R. and Klein, S. A.: Low Cloud Type over the Ocean from Surface Observations. Part III: Relationship to Vertical Motion and the Regional Surface Synoptic Environment, Journal of Climate, 13, 245–256, https://doi.org/10.1175/1520-0442(2000)013<0245:LCTOTO>2.0.CO;2, 2000.

O'Connor, E. J., Hogan, R. J., and Illingworth, A. J.: Retrieving Stratocumulus Drizzle Parameters Using Doppler Radar and Lidar, Journal of Applied Meteorology, 44, 14–27, https://doi.org/10.1175/JAM-2181.1, 2005.

Prein, A. F., Langhans, W., Fosser, G., Ferrone, A., Ban, N., Goergen, K., Keller, M., Tölle, M., Gutjahr, O., Feser, F., Brisson, E., Kollet, S., Schmidli, J., Van Lipzig, N. P. M., and Leung, R.: A review on regional convection-permitting climate modeling: Demonstrations, prospects, and challenges, Reviews of Geophysics, 53, 323–361, https://doi.org/10.1002/2014RG000475, 2015.

Riihimaki, L., Sivaraman, C., and Zhang, D.: Planetary Boundary Layer Height (PBLHTSONDE1MCFARL), https://doi.org/10.5439/1991783, 2013.

Rutledge, S. A. and Hobbs, P.: The Mesoscale and Microscale Structure and Organization of Clouds and Precipitation in Midlatitude Cyclones. VIII: A Model for the "Seeder-Feeder" Process in Warm-Frontal Rainbands, Journal of the Atmospheric Sciences, 40, 1185–1206, https://doi.org/10.1175/1520-0469(1983)040<1185:TMAMSA>2.0.CO;2, 1983.

Rémillard, J. and Tselioudis, G.: Cloud Regime Variability over the Azores and Its Application to Climate Model Evaluation, Journal of Climate, 28, 9707–9720, https://doi.org/10.1175/JCLI-D-15-0066.1, 2015.

Rémillard, J., Kollias, P., Luke, E., and Wood, R.: Marine Boundary Layer Cloud Observations in the Azores, Journal of Climate, 25, 7381–7398, https://doi.org/10.1175/JCLI-D-11-00610.1, 2012.

Rémillard, J., Fridlind, A. M., Ackerman, A. S., Tselioudis, G., Kollias, P., Mechem, D. B., Chandler, H. E., Luke, E., Wood, R., Witte, M. K., Chuang, P. Y., and Ayers, J. K.: Use of Cloud Radar Doppler Spectra to Evaluate Stratocumulus Drizzle Size Distributions in Large-Eddy Simulations with Size-Resolved Microphysics, Journal of Applied Meteorology and Climatology, 56, 3263–3283, https://doi.org/10.1175/JAMC-D-17-0100.1, 2017.

Savic-Jovcic, V. and Stevens, B.: The Structure and Mesoscale Organization of Precipitating Stratocumulus, Journal of the Atmospheric Sciences, 65, 1587–1605, https://doi.org/10.1175/2007JAS2456.1, 2008.

Simmonds, I., Keay, K., and Tristram Bye, J. A.: Identification and Climatology of Southern Hemisphere Mobile Fronts in a Modern Reanalysis, Journal of Climate, 25, 1945–1962, https://doi.org/10.1175/JCLI-D-11-00100.1, 2012.

Sinclair, V. A., Belcher, S. E., and Gray, S. L.: Synoptic Controls on Boundary-Layer Characteristics, Boundary-Layer Meteorology, 134, 387–409, https://doi.org/10.1007/s10546-009-9455-6, 2010.

Slingo, J. M.: The Development and Verification of A Cloud Prediction Scheme For the Ecmwf Model, Quarterly Journal of the Royal Meteorological Society, 113, 899–927, https://doi.org/10.1002/qj.49711347710, 1987.

Stein, U. and Alpert, P.: Factor Separation in Numerical Simulations, Journal of the Atmospheric Sciences, 50, 2107–2115, https://doi.org/10.1175/1520-0469(1993)050<2107:FSINS>2.0.CO;2, 1993.

Stevens, B., Cotton, W. R., Feingold, G., and Moeng, C.-H.: Large-Eddy Simulations of Strongly Precipitating, Shallow, Stratocumulus-Topped Boundary Layers, Journal of the Atmospheric Sciences, 55, 3616–3638, https://doi.org/10.1175/1520-0469(1998)055<3616:LESOSP>2.0.CO;2, 1998.

Stevens, B., Moeng, C.-H., Ackerman, A. S., Bretherton, C. S., Chlond, A., De Roode, S., Edwards, J., Golaz, J.-C., Jiang, H., Khairoutdinov, M., Kirkpatrick, M. P., Lewellen, D. C., Lock, A., Müller, F., Stevens, D. E., Whelan, E., and Zhu, P.: Evaluation of Large-Eddy Simulations via Observations of Nocturnal Marine Stratocumulus, Monthly Weather Review, 133, 1443–1462, https://doi.org/10.1175/MWR2930.1, 2005.

Thompson, G., Field, P. R., Rasmussen, R. M., and Hall, W. D.: Explicit Forecasts of Winter Precipitation Using an Improved Bulk Microphysics Scheme. Part II: Implementation of a New Snow Parameterization, Monthly Weather Review, 136, 5095–5115, https://doi.org/10.1175/2008MWR2387.1, 2008.

Tiedtke, M., Heckley, W. A., and Slingo, J.: Tropical forecasting at ECMWF: The influence of physical parametrization on the mean structure of forecasts and analyses, Quarterly Journal of the Royal Meteorological Society, 114, 639–664, https://doi.org/10.1002/qj.49711448106, 1988.

Turner, D. D.: Improved ground-based liquid water path retrievals using a combined infrared and microwave approach, Journal of Geophysical Research: Atmospheres, 112, 2007JD008 530, https://doi.org/10.1029/2007JD008530, 2007.

vanZanten, M. C., Stevens, B., Nuijens, L., Siebesma, A. P., Ackerman, A. S., Burnet, F., Cheng, A., Couvreux, F., Jiang, H., Khairoutdinov, M., Kogan, Y., Lewellen, D. C., Mechem, D., Nakamura, K., Noda, A., Shipway, B. J., Slawinska, J., Wang, S., and Wyszogrodzki, A.: Controls on precipitation and cloudiness in simulations of trade-wind cumulus as observed during RICO: CONTROLS ON PRECIPITATION … IN TRADE-WIND CUMULUS, Journal of Advances in Modeling Earth Systems, 3, n/a–n/a, https://doi.org/10.1029/2011MS000056, 2011.

Wang, J., Rossow, W. B., Uttal, T., and Rozendaal, M.: Variability of Cloud Vertical Structure during ASTEX Observed from a Combination of Rawinsonde, Radar, Ceilometer, and Satellite, Monthly Weather Review, 127, 2484–2502, https://doi.org/10.1175/1520-0493(1999)127<2484:VOCVSD>2.0.CO;2, 1999.

Wang, J., Wood, R., Jensen, M. P., Chiu, J. C., Liu, Y., Lamer, K., Desai, N., Giangrande, S. E., Knopf, D. A., Kollias, P., Laskin, A., Liu, X., Lu, C., Mechem, D., Mei, F., Starzec, M., Tomlinson, J., Wang, Y., Yum, S. S., Zheng, G., Aiken, A. C., Azevedo, E. B., Blanchard, Y., China, S., Dong, X., Gallo, F., Gao, S., Ghate, V. P., Glienke, S., Goldberger, L., Hardin, J. C., Kuang, C., Luke, E. P., Matthews, A. A., Miller, M. A., Moffet, R., Pekour, M., Schmid, B., Sedlacek, A. J., Shaw, R. A., Shilling, J. E., Sullivan, A., Suski, K., Veghte, D. P., Weber, R., Wyant, M., Yeom, J., Zawadowicz, M., and Zhang, Z.: Aerosol and Cloud Experiments in the Eastern North Atlantic (ACE-ENA), Bulletin of the American Meteorological Society, 103, E619–E641, https://doi.org/10.1175/BAMS-D-19-0220.1, 2022.

Wang, S., O'Neill, L. W., Jiang, Q., De Szoeke, S. P., Hong, X., Jin, H., Thompson, W. T., and Zheng, X.: A regional real-time forecast of marine boundary layers during VOCALS-REx, Atmospheric Chemistry and Physics, 11, 421–437, https://doi.org/10.5194/acp-11-421-2011, 2011.

Weisman, M. L., Skamarock, W. C., and Klemp, J. B.: The Resolution Dependence of Explicitly Modeled Convective Systems, Monthly Weather Review, 125, 527–548, https://doi.org/10.1175/1520-0493(1997)125<0527:TRDOEM>2.0.CO;2, 1997.

Wood, R. and Bretherton, C. S.: Boundary Layer Depth, Entrainment, and Decoupling in the Cloud-Capped Subtropical and Tropical Marine Boundary Layer, Journal of Climate, 17, 3576–3588, https://doi.org/10.1175/1520-0442(2004)017<3576:BLDEAD>2.0.CO;2, 2004.

Wood, R. and Bretherton, C. S.: On the Relationship between Stratiform Low Cloud Cover and Lower-Tropospheric Stability, Journal of Climate, 19, 6425–6432, https://doi.org/10.1175/JCLI3988.1, 2006.

Wood, R., Wyant, M., Bretherton, C. S., Rémillard, J., Kollias, P., Fletcher, J., Stemmler, J., De Szoeke, S., Yuter, S., Miller, M., Mechem, D., Tselioudis, G., Chiu, J. C., Mann, J. A. L., O'Connor, E. J., Hogan, R. J., Dong, X., Miller, M., Ghate, V., Jefferson, A., Min, Q., Minnis, P., Palikonda, R., Albrecht, B., Luke, E., Hannay, C., and Lin, Y.: Clouds, Aerosols, and Precipitation in the Marine Boundary Layer: An Arm Mobile Facility Deployment, Bulletin of the American Meteorological Society, 96, 419–440, https://doi.org/10.1175/BAMS-D-13-00180.1, 2015.

Wyant, M. C., Wood, R., Bretherton, C. S., Mechoso, C. R., Bacmeister, J., Balmaseda, M. A., Barrett, B., Codron, F., Earnshaw, P., Fast, J., Hannay, C., Kaiser, J. W., Kitagawa, H., Klein, S. A., Köhler, M., Manganello, J., Pan, H.-L., Sun, F., Wang, S., and Wang, Y.: The PreVOCA experiment: modeling the lower troposphere in the Southeast Pacific, Atmospheric Chemistry and Physics, 10, 4757–4774, https://doi.org/10.5194/acp-10-4757-2010, 2010.

Wyant, M. C., Bretherton, C. S., Wood, R., Carmichael, G. R., Clarke, A., Fast, J., George, R., Gustafson Jr., W. I., Hannay, C., Lauer, A., Lin, Y., Morcrette, J.-J., Mulcahy, J., Saide, P. E., Spak, S. N., and Yang, Q.: Global and regional modeling of clouds and aerosols in the marine boundary layer during VOCALS: the VOCA intercomparison, Atmospheric Chemistry and Physics, 15, 153–172, https://doi.org/10.5194/acp-15-153-2015, 2015.

Yau, M. K. and Rogers, R. R.: A Short Course in Cloud Physics, Elsevier Science, Saint Louis, 3rd ed edn., ISBN 978-0-08-057094-5, oCLC: 1038784231, 1996.

Zelinka, M. D., Zhou, C., and Klein, S. A.: Insights from a refined decomposition of cloud feedbacks, Geophysical Research Letters, 43, 9259–9269, https://doi.org/10.1002/2016GL069917, 2016.

Zelinka, M. D., Myers, T. A., McCoy, D. T., Po-Chedley, S., Caldwell, P. M., Ceppi, P., Klein, S. A., and Taylor, K. E.: Causes of Higher Climate Sensitivity in CMIP6 Models, Geophysical Research Letters, 47, e2019GL085 782, https://doi.org/10.1029/2019GL085782, 2020.

Zuidema, P., Westwater, E. R., Fairall, C., and Hazen, D.: Ship-based liquid water path estimates in marine stratocumulus, Journal of Geophysical Research: Atmospheres, 110, 2005JD005 833, https://doi.org/10.1029/2005JD005833, 2005.

Table 1. List of COAMPS sensitivity simulations run. Each sensitivity simulation is a variation of the control simulation, with the modifications noted.

Microphysics parameterization	N_r, N_c constants	Number of vertical grid points	Purpose
KK Lite	N_r=0.01, N_c=100	45	control
Kessler		45	microphysics parameterization sensitivity
Thompson		45	microphysics parameterization sensitivity
KK Lite	N_r=0.01, N_c=40	45	N_c sensitivity
KK Lite	N_r=0.1, N_c=100	45	N_r sensitivity
KK Lite	N_r=0.1, N_c=40	45	N_r, N_c mutual interaction sensitivity
KK Lite	N_r=0.1, N_c=100	87	vertical grid sensitivity

Table 2. Cloud-conditioned ENA means (top values) and fine mesh domain means (edge points of fine mesh removed) (bottom values in italics) for each microphysics parameterization and observations during the northerly wind period of the case study.

	Observed	Kessler	Thompson	KK Lite	KK Lite N_c=40, N_r=0.01	KK Lite N_c=100, N_r=0.1	KK Lite N_c=40, N_r=0.1
Cloud base RR (mm d^{-1})	6.06	1.63 *2.98*	1.45 *1.72*	1.82 *8.18*	2.65 *8.36*	0.40 *2.65*	0.67 *2.85*
Surface RR (mm d^{-1})	0.87	0.75 *2.23*	0.27 *1.04*	0.61 *6.14*	1.06 *6.12*	0.02 *1.56*	0.09 *1.62*
Sub-cloud evaporation rate (mm d^{-1})	5.17	0.88 *0.75*	1.17 *0.67*	1.21 *2.04*	1.59 *2.24*	0.38 *1.09*	0.58 *1.22*
PBL depth (m)	1746.8	1388.1 *1153.4*	1519.4 *1243.1*	1375.3 *1139.6*	1383.4 *1140.0*	1439.0 *1142.1*	1393.6 *1133.9*
LWP (g m^{-2})	55.3	54.2 *39.6*	127.3 *92.4*	113.3 *97.4*	119.0 *92.8*	201.6 *133.7*	191.8 *127.6*
Cloud thickness (m)	294.7	351.5 *336.9*	500.1 *538.4*	434.5 *446.9*	442.8 *434.1*	521.3 *496.5*	517.7 *483.4*
Low cloud cover (%)	76.1	84.6 *74.8*	87.4 *74.1*	81.5 *71.8*	82.9 *72.6*	85.5 *73.9*	81.6 *74.4*

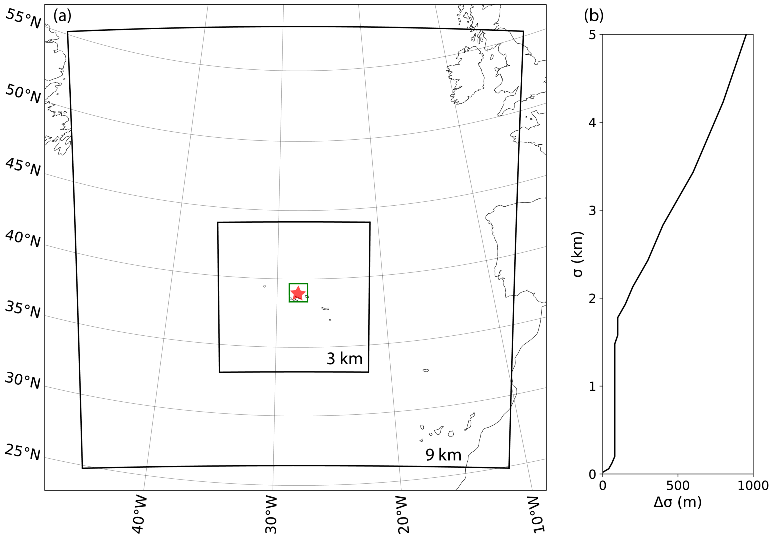

Figure 1. (a) COAMPS doubly nested domain centered on Graciosa Island (red star). The 144 km × 144 km analysis box is outlined in green. (b) COAMPS vertical grid spacing ($\Delta\sigma$) with height (σ) over the lowest 5 km.

https://doi.org/10.5194/egusphere-2024-3438
Preprint. Discussion started: 13 January 2025

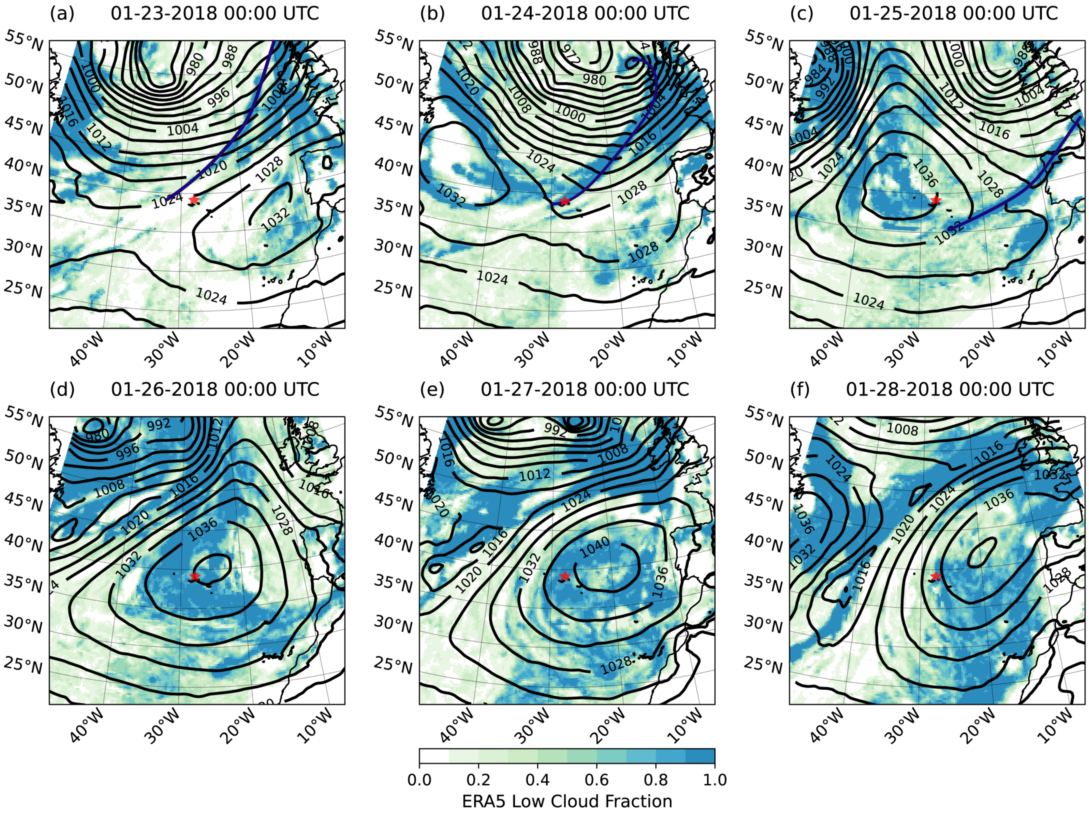

Figure 2. ERA5 SLP (black contours), low cloud fraction (color-filled contours) in the north Atlantic at 00:00 UTC 23-28 January 2018. Graciosa Island is marked by the red start, and the cold front is shown by the dark blue line.

https://doi.org/10.5194/egusphere-2024-3438
Preprint. Discussion started: 13 January 2025

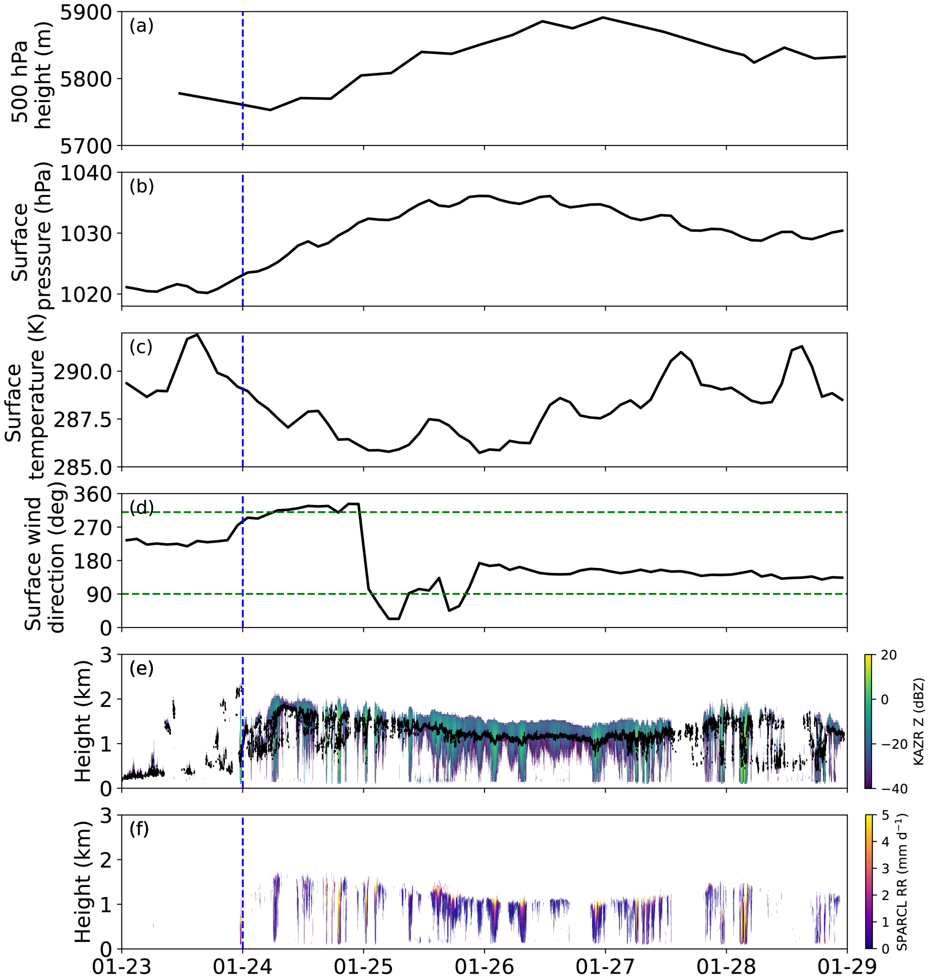

Figure 3. ENA observations over the simulation period (23-28 January 2018). (a) 500 hPa heights from the soundings, (b) MET surface pressure, (c) MET surface temperature, (d) MET surface wind direction, (e) KAZR radar reflectivity and ceilometer cloud base height, (f) SPARCL sub-cloud drizzle rates. The passage of the cold front is shown by the vertical blue line.

https://doi.org/10.5194/egusphere-2024-3438
Preprint. Discussion started: 13 January 2025

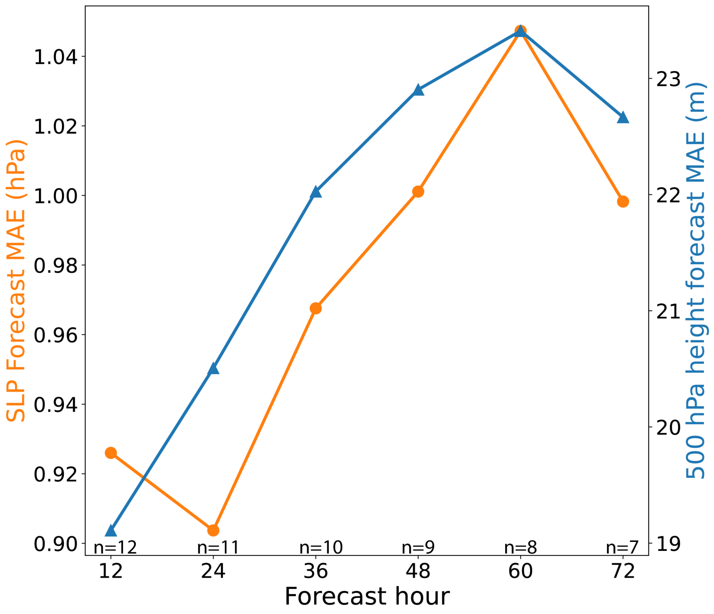

Figure 4. SLP (blue) and 500 hPa geopotential height (purple) MAE (compared to ERA5) versus the forecast hour for a series of simulations. The number of simulations (n) included in the MAE calculation for each forecast hour is listed.

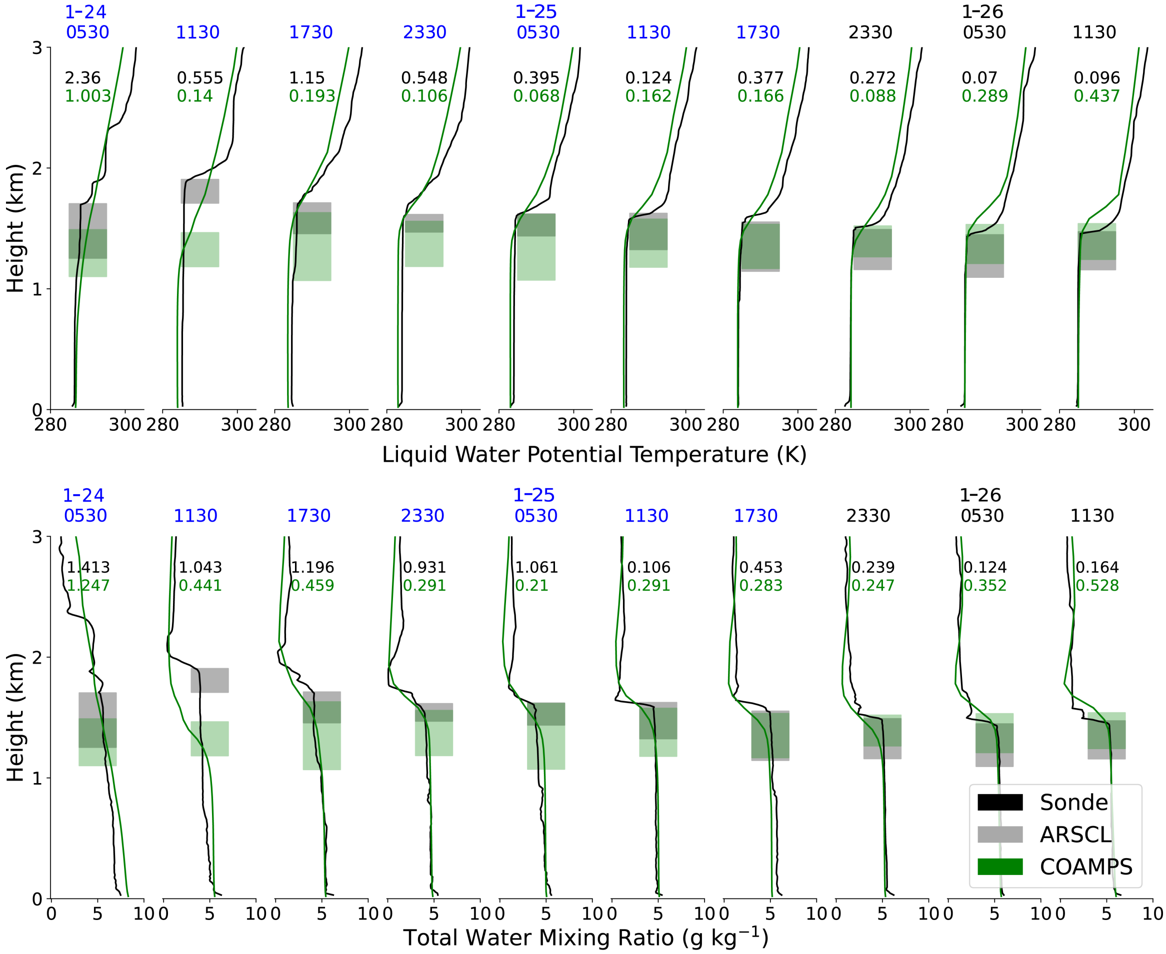

Figure 5. Liquid water potential temperature (top row) and total water mixing ration (bottom row) profiles from sounding (black) and the COAMPS control simulation (green) throughout the study period. ARSCL cloud boundaries are colored light grey, COAMPS cloud boundaries are colored green, and the overlap between the two is dark green. The blue dates indicate the soundings taken during the northerly wind period and the black dates are from the southerly wind period. Numbers at the top of each plot indicate the decoupling index calculated from the sounding (black) and COAMPS (green) liquid water potential temperature (top row) and total water mixing ratio (bottom) profiles.

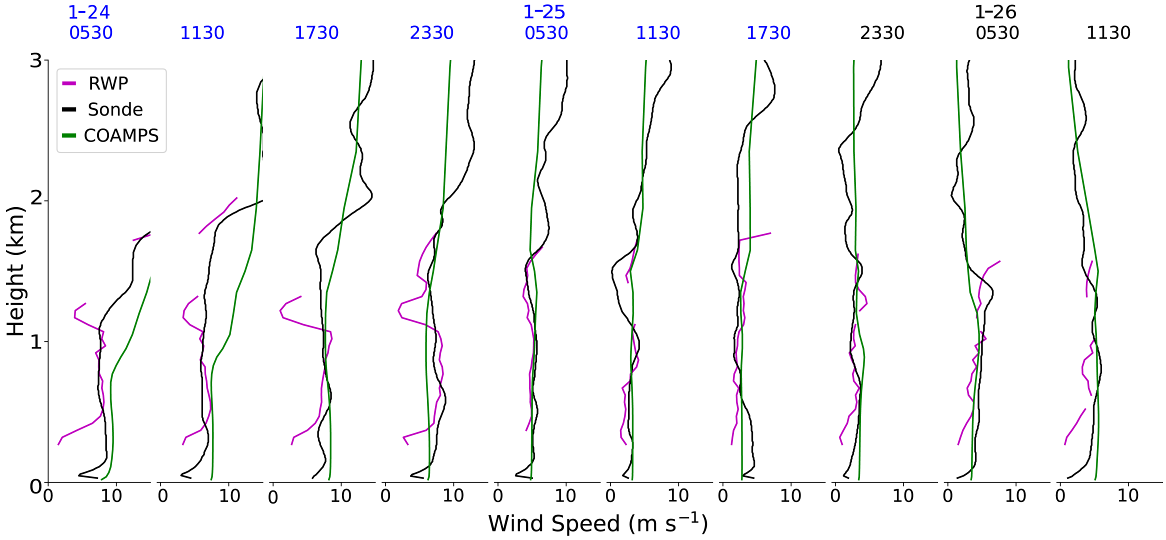

Figure 6. Same as Fig. 5 but for profiles of Radar Wind Profiler, sounding, and COAMPS wind speeds.

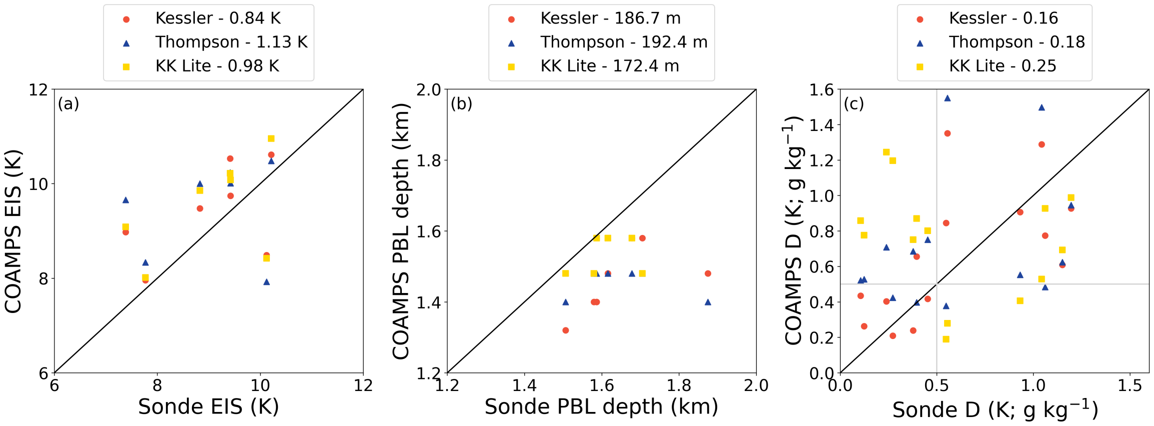

Figure 7. COAMPS vs sounding (a) stability (EIS), (b) PBL depth, and (c) decoupling parameters calculated from both the liquid water potential temperature and total water mixing ration profiles during the northerly wind period of the case study (7 total soundings). The 1:1 line is plotted in black and the MAE between the observed and each COAMPS microphysics scheme is listed in the legend.

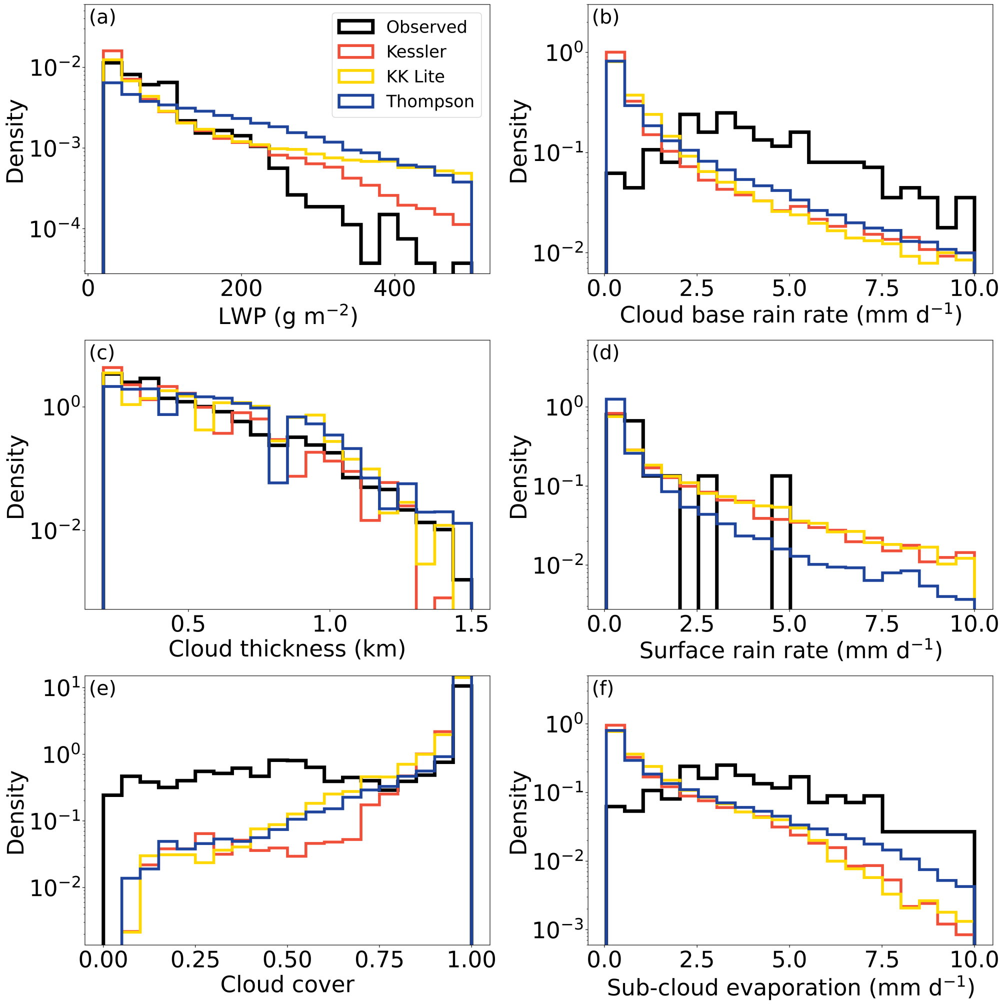

Figure 8. PDF of observations (black) and each microphysics scheme during the northerly wind period of the case study.

https://doi.org/10.5194/egusphere-2024-3438
Preprint. Discussion started: 13 January 2025

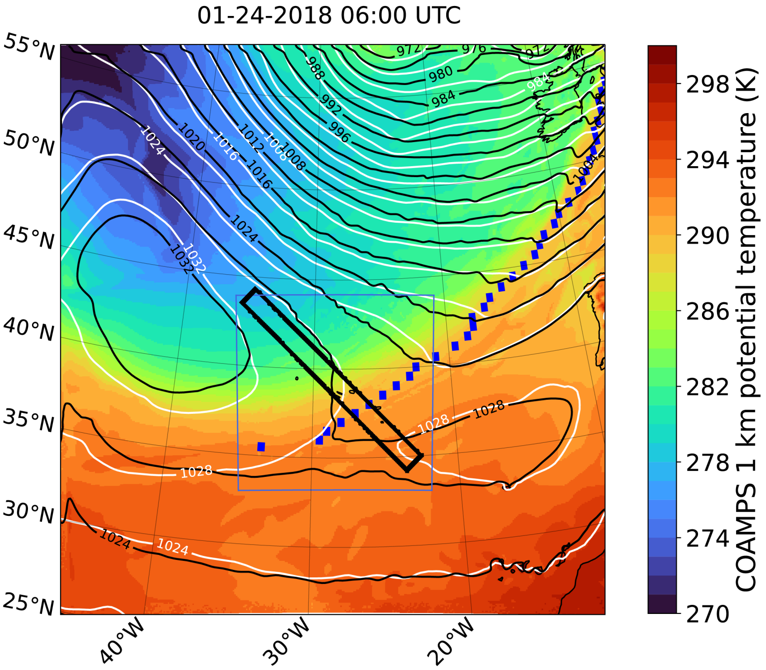

Figure 9. COAMPS coarse mesh SLP (black contours) and 1 km potential temperature (color-filled contours), ERA5 SLP (white contours), and identified cold front (blue dots). The outline of the fine mesh is the blue box, and the transect width is outlined by the thick black lines.

https://doi.org/10.5194/egusphere-2024-3438
Preprint. Discussion started: 13 January 2025

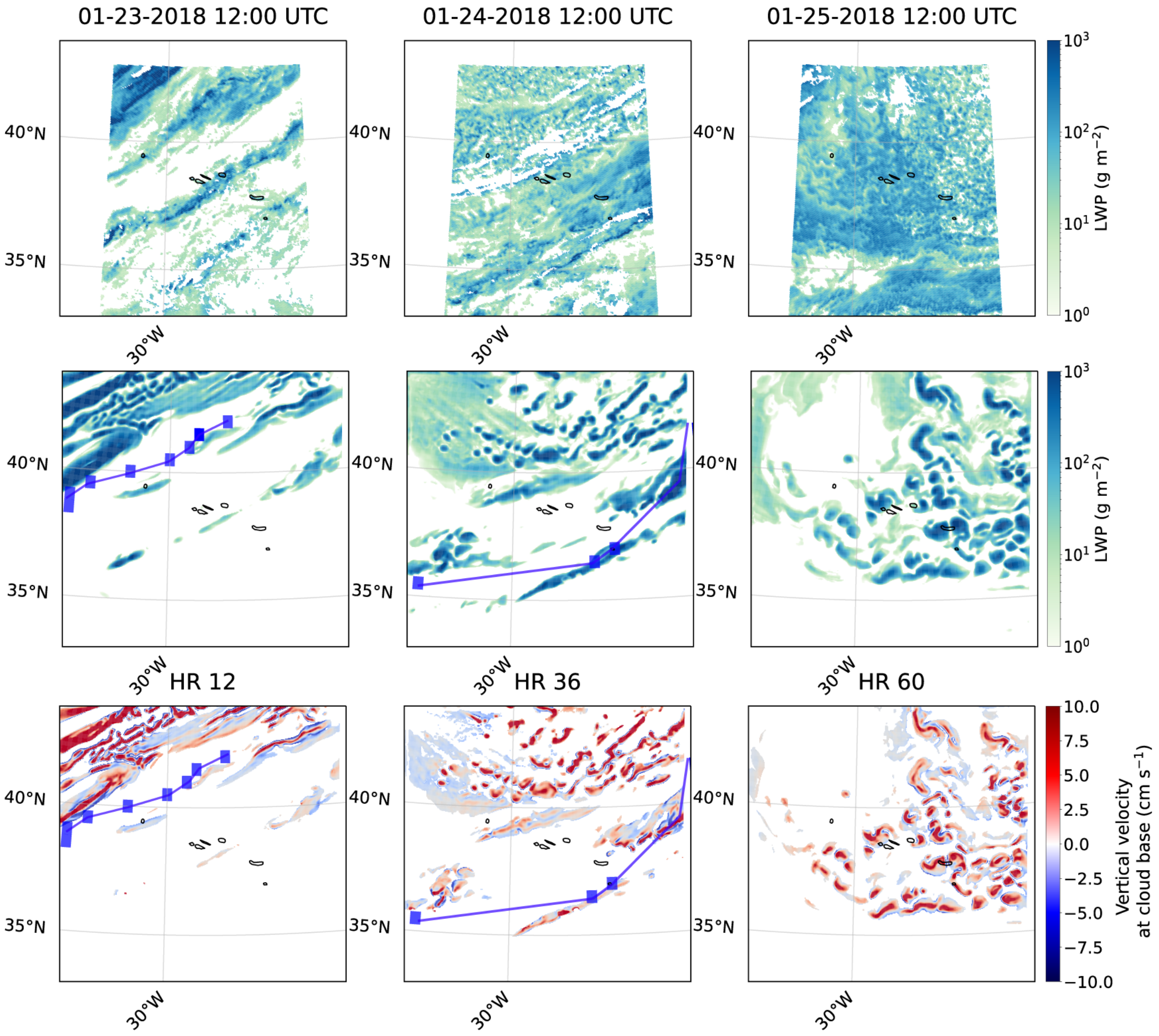

Figure 10. Satellite-derived LWP (top row), COAMPS LWP (middle row), and COAMPS cloud base vertical velocity (bottom row) for 12:00 UTC on 23 January (left column), 24 January (middle column), and 25 January 2018 (right column) and the equivalent COAMPS forecast time. The location of the algorithm-identified cold front is shown by the blue squares and lines.

https://doi.org/10.5194/egusphere-2024-3438
Preprint. Discussion started: 13 January 2025

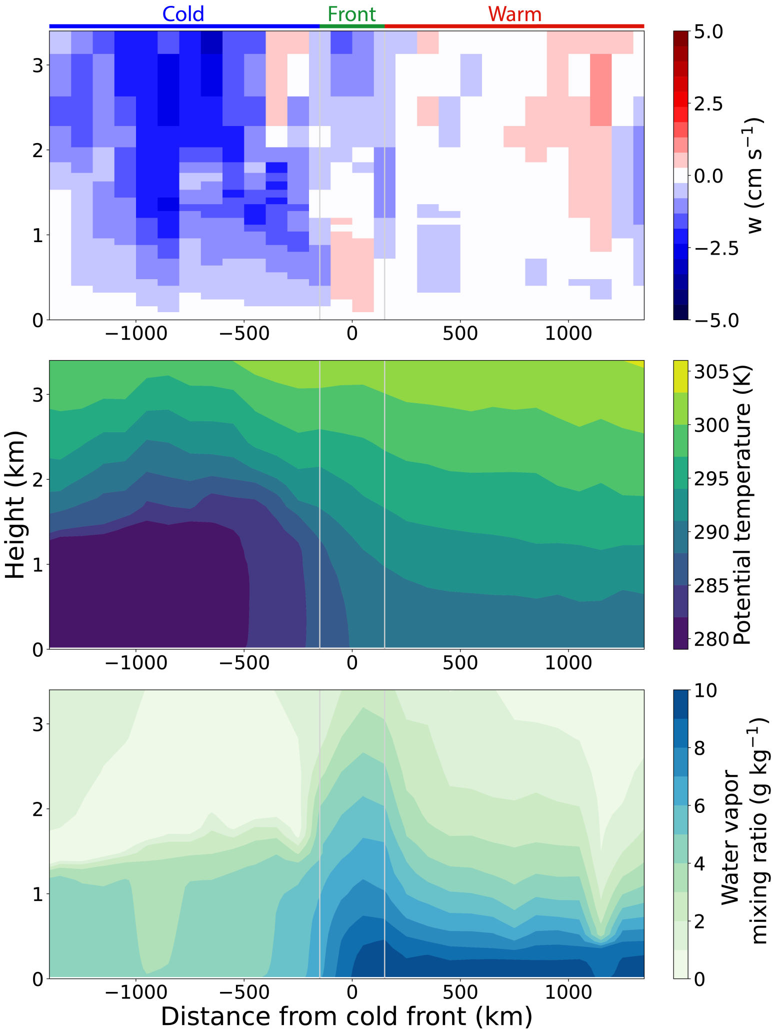

Figure 11. Vertical cross sections along the transect of the median of 8 model forecast times of (top) vertical motion, (middle) potential temperature, and (bottom) water vapor mixing ratio. The 0 distance marks the location of the cold front.

https://doi.org/10.5194/egusphere-2024-3438
Preprint. Discussion started: 13 January 2025

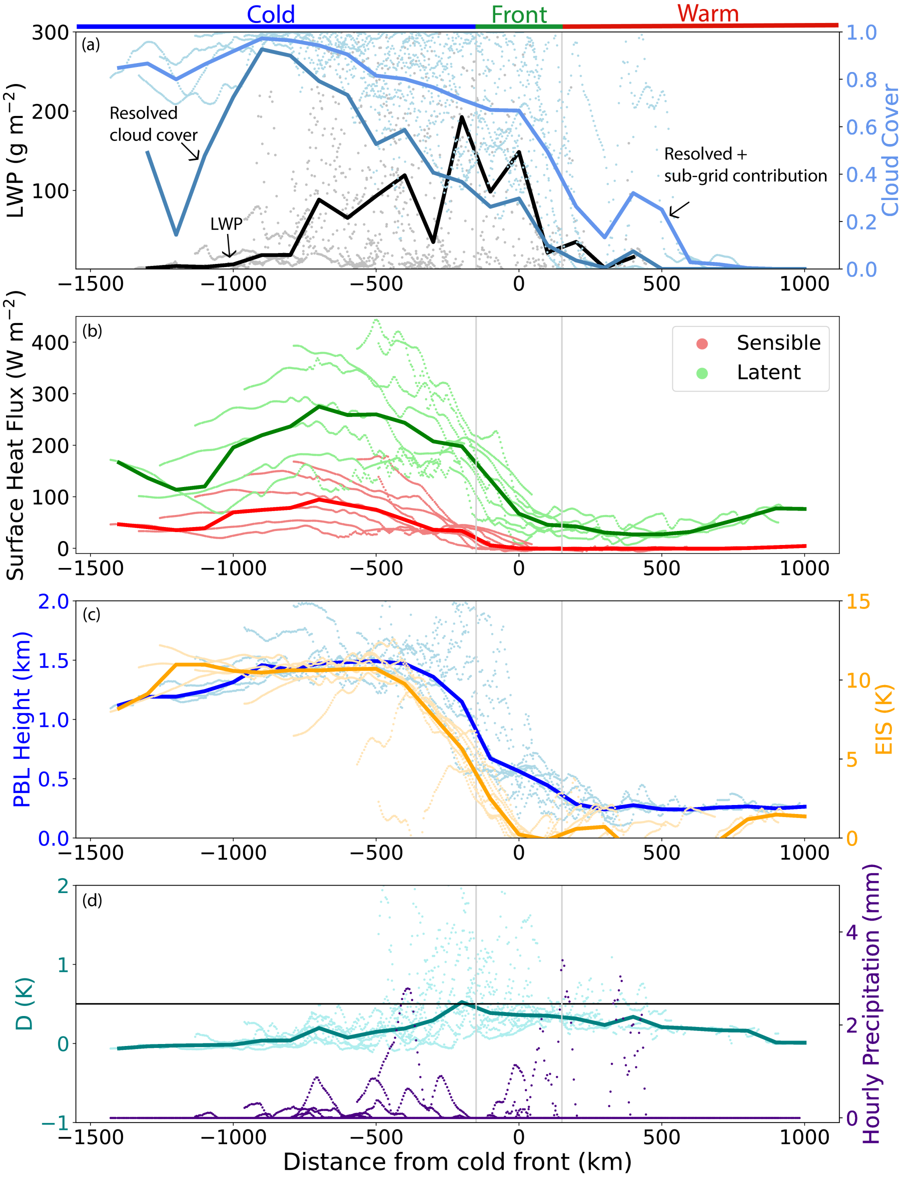

Figure 12. Cold-front-centered transects for 8 different forecast hours (forecast hours 12, 18, 24, 30, 36, 42, 48, and 54). Thin lines or dots represent each transect at a given time and the thicker lines represent the median in 100 km bins of all composites. LWP is conditioned on non-zero values.

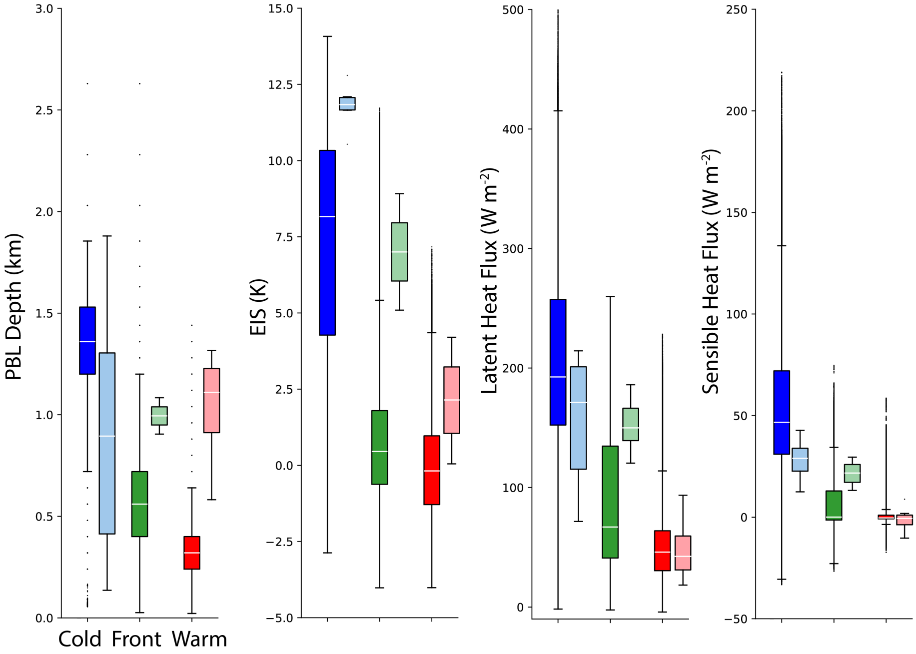

Figure 13. Box plots of COAMPS environmental variables (darker colors) and observations (lighter colors) in each the cold (blue), frontal (green), and warm (red) sectors.

https://doi.org/10.5194/egusphere-2024-3438
Preprint. Discussion started: 13 January 2025

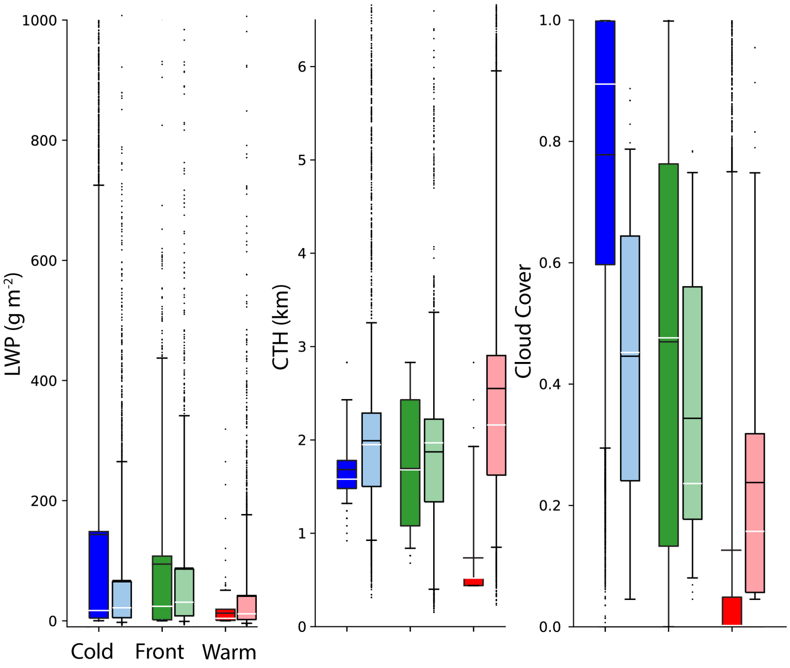

Figure 14. Box plots of COAMPS cloud variables (darker colors) and satellite observations (lighter colors) in each the cold (blue), frontal (green), and warm (red) sectors. Median values are shown by the white line, and mean values are the black line. LWP is conditioned on non-zero values and COAMPS cloud cover includes the sub-grid contribution.

https://doi.org/10.5194/egusphere-2024-3438
Preprint. Discussion started: 13 January 2025

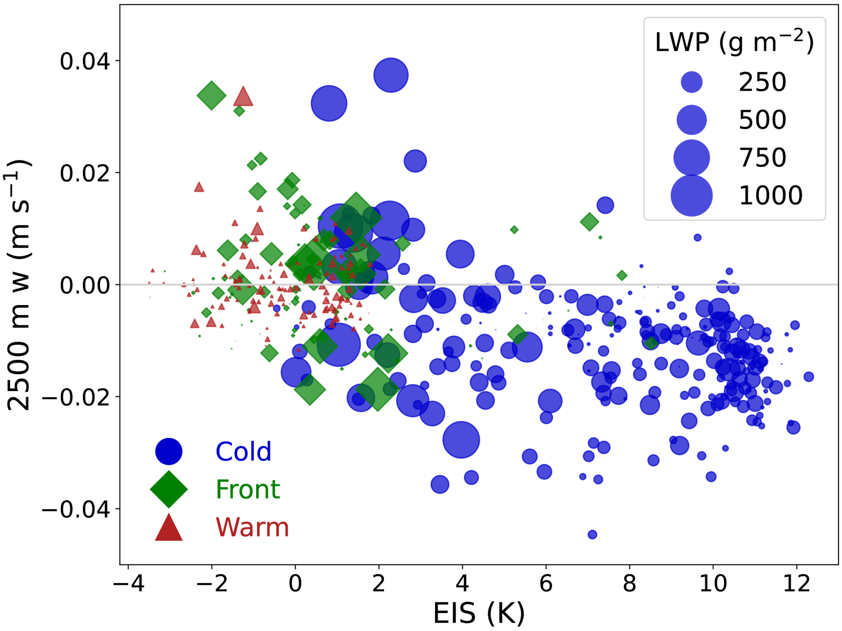

Figure 15. 2500 m vertical velocity versus EIS, color-coded and shaped by the sector: cold (blue circles), warm (red triangles), and frontal (green diamonds). The size of the marker indicates the LWP for all shapes. Each marker represents the average of 144 × 144 km boxes throughout the fine mesh at 8 different forecast hours.